Dan Golomb

NRL Memorandum Report 3083

Coupled Barium Cloud-Ionosphere Systems

4. Striation Penetration into an Inhomogeneous Ionosphere

S. R. GOLDMAN AND A. J. SCANNAPIECO

Science Applications Inc.
McLean, Virginia 22101

and

L. BAKER AND S. L. OSSAKOW

Plasma Applications Branch
Plasma Physics Division

July 1975 D/C

This work was supported by the Defense Nuclear Agency
under Subtask No. HC041

NAVAL RESEARCH LABORATORY
Washington, D.C.

REPORT DOCUMENTATION PAGE

READ INSTRUCTIONS BEFORE COMPLETING FORM

1. REPORT NUMBER: NRL Memorandum Report 3083	2. GOVT ACCESSION NO.
3. RECIPIENT'S CATALOG NUMBER	
4. TITLE (and Subtitle): COUPLED BARIUM CLOUD-IONOSPHERE SYSTEMS 4. STRIATION PENETRATION INTO AN INHOMOGENEOUS IONOSPHERE	5. TYPE OF REPORT & PERIOD COVERED: Interim Report on a continuing NRL problem
	6. PERFORMING ORG. REPORT NUMBER
7. AUTHOR(s): S.R. Goldman, SAI, L. Baker, S.L. Ossakow, and A.J. Scannapieco, SAI	8. CONTRACT OR GRANT NUMBER(s)
9. PERFORMING ORGANIZATION NAME AND ADDRESS: Naval Research Laboratory, Washington, D.C. 20375	10. PROGRAM ELEMENT, PROJECT, TASK AREA & WORK UNIT NUMBERS: NRL Problem H02-27B; DNA Subtask S99QAXHC041
11. CONTROLLING OFFICE NAME AND ADDRESS: Defense Nuclear Agency, Washington, D.C. 20305	12. REPORT DATE: July 1975
	13. NUMBER OF PAGES: 98
14. MONITORING AGENCY NAME & ADDRESS (if different from Controlling Office)	15. SECURITY CLASS. (of this report): Unclassified
	15a. DECLASSIFICATION/DOWNGRADING SCHEDULE

16. DISTRIBUTION STATEMENT (of this Report)

Approved for public release; distribution unlimited.

17. DISTRIBUTION STATEMENT (of the abstract entered in Block 20, if different from Report)

18. SUPPLEMENTARY NOTES

This work was supported by the Defense Nuclear Agency under Subtask No. HC041.

19. KEY WORDS (Continue on reverse side if necessary and identify by block number)

Striations
Inhomogeneous Ionosphere
Potential Variation along magnetic field

20. ABSTRACT (Continue on reverse side if necessary and identify by block number)

The present study investigates, via linear theory, how striations (treated as perturbations) created in a plasma cloud, centered at 200 km, will penetrate into the background inhomogeneous (real) ionosphere as a function of wavelength, integrated Pedersen conductivity ratio of the cloud to ionosphere (Σ_p^b/Σ_p^i), and ambient ionospheric conditions. The study is posed as an eigenvalue problem which while determining the potential variation (eigenmode) along magnetic field lines, self-consistently solves for the growth rate (eigenvalue) in the coupled cloud-inhomogeneous ionospheric system. Perturbed particle densities, fluxes parallel to the

(Continued)

magnetic field, B, and electrostatic potential are presented as a function of altitude. The results show the importance of the image transport parameter $(kL_{\perp}\nu_i/\omega_{ci})(1+\nu_i{}^2/\omega_{ci}{}^2)^{-1}$ (where k is the wavenumber transverse to B, $L_{\perp}$ is the transverse dimension of the cloud, and ν_i and ω_{ci} are the ionospheric ion-neutral collision frequency and ion cyclotron frequency, respectively) in determining the magnitude of imaging and aspect angle of striations with respect to B (i.e., striations take on a parallel component of wavenumber). Perturbations penetrate further down in the presence of the plasma cloud than in simple previous studies which neglected image transport and considered the perturbation mapping from one region of the ionosphere to another. Our results show that clouds with smaller conductivity ratios produce image striations further down into the background E region ionosphere with a more uniform coupling as a function of wavelength. It is also shown that there is a slight dependence of the E region coupling of the perturbations on the level of solar activity (solar maximum or minimum conditions) and also this E region coupling shows a slight dependence on the extent of F region coupling above the cloud. Finally, with our best estimates for F region coupling, the growth rates show negligible short wavelength damping due to ionospheric coupling for the $\Sigma_p^b/\Sigma_p^i = 4$ case; whereas, for the $\Sigma_p^b/\Sigma_p^i = 0.2$ case the ionospheric coupling is significant with respect to structuring the spectrum at short wavelengths.

CONTENTS

COUPLED BARIUM CLOUD-IONOSPHERE SYSTEMS
4. STRIATION PENETRATION INTO AN INHOMOGENEOUS IONOSPHERE

I. Introduction

In the past few years much theoretical and computational work has been devoted towards understanding the behavior of striations produced by barium clouds released in the ionosphere [Linson and Workman, 1970; Simon, 1970; Völk and Haerendel, 1971; Simon and Sleeper, 1972; Perkins et al., 1973; Zabusky et al., 1973; Lloyd and Haerendel, 1973; Shiau and Simon, 1973; Goldman et al., 1974, Scannapieco et al., 1974; and Perkins and Doles, 1975]. In studying striation growth coupled to the background ionosphere it is important to know how the induced potential (or electric field transverse to the magnetic field) varies along the magnetic field line as one moves away from the localized region of the barium cloud. Some investigators [Farley, 1959, 1960; Spreiter and Briggs, 1961; Swift, 1972] have treated the related problem of mapping transverse sinusoidal, spatially varying electric fields produced in one region of the ionosphere to other regions. These works characteristically neglect the density induced by the presence of these electric fields on the mapping (imaging) of these electric fields. Moreover, the mechanism producing the primary electric fields is not considered (a static problem is investigated, i.e., no time variation of the fields). Nevertheless, such studies have shown in detail [Farley, 1959, 1960; Spreiter and Briggs, 1961] that for transverse wavelengths $\geqslant$ 1 km the magnetic field lines act as equipotentials, i.e., shorter wavelength electric field perturbations don't couple effectively from one region of the ionosphere to another.

Note: Manuscript submitted June 24, 1975.

Most ideas about the potential variation along magnetic field lines, as a function of transverse wavelength, are based on these earlier works. Moreover, the multilevel, two-dimensional theoretical and numerical simulation studies of barium clouds coupled to the background ionosphere [Lloyd and Haerendel, 1973; Goldman et al.; 1974, Scannapieco et al., 1974] have assumed that the electric fields at the cloud level and the background ionosphere are the same. That is, the electric fields have only transverse spatial dependence in the two dimensions perpendicular to the magnetic field and no variation along the magnetic field lines. Estimates of striation behavior, based on linear theory and including coupling to the background ionosphere, have been done by Völk and Haerendel [1971], and Perkins et al. [1973]. However, both sets of authors have assumed that the ionosphere is uniform, though different in density and Pedersen conductivity from the barium cloud (inhomogeneity region). Also, high altitude models were used, i.e., the ratio of ion-neutral collision frequency to ion cyclotron frequency, ν/ω_c, was assumed small for both the cloud and ionosphere. Indeed, in the section on "image striations in a homogeneous background" in Völk and Haerendel [1971], simple conclusions are drawn based upon the simplifying assumptions of homogeneous ionosphere and equal ν/ω_c for the barium cloud and the ionosphere. Although these assumptions may be valid for potential modes which are localized along the magnetic field lines in the vicinity of the barium cloud, they are not in general valid. Völk and Haerendel [1971] state that the results of their

simplified analysis on image effects on striation growth show the need for considering a real ionosphere. Swift [1972] has also noted that his results and essentially those of Farley [1959, 1960] and Spreiter and Briggs [1961] have to viewed with caution when transverse inhomogeneities (e.g., barium clouds) are present.

With all this in mind, the purpose of the present study is to assess the interaction between the earth's ionosphere and striations which are generated in a relatively localized region of the ionosphere by density gradients in a barium cloud. Our study is posed as an eigenvalue problem which while determining how far (along the magnetic field) striations, created in a barium cloud, will penetrate into the background inhomogeneous ionosphere also, self-consistently, solves for their growth rate. All this is done as a function of transverse wavelength, Pedersen conductivity ratio (cloud to ionosphere), and ambient ionospheric conditions (for real ionospheres). For cases where the integrated Pedersen conductivity of the barium cloud, Σ_p^b, is large compared to the integrated Pedersen conductivity of the background ionosphere, Σ_p^i, the growth rate of the instability depends on barium cloud parameters and is essentially known. However, the self-consistent imaging at different altitudes in the ionosphere has not been fully treated. For cases where Σ_p^b is comparable to or smaller that Σ_p^i neither the striation growth or the self-consistent imaging has been fully treated.

We present in the second section the model and theory; in the third section numerical results and discussion of the eigenmodes and

eigenvalues and modifications due to partial coupling to the F region; and in the fourth section summary and conclusions.

II. Model and Theory

In our model the magnetic field, $\underline{B}$, is taken to be vertical and in the z direction. Furthermore, the barium cloud is taken to be localized in z at altitudes high enough so that one does not have to be concerned with the variation of the electrostatic potential over its length along z. Also, there is a spatially and temporally constant background ambient electric field, $\underline{E}_o$ and neutral winds are neglected.

At each point in space the electron and ion densities, n, assumed equal under the standard long wavelength (quasi-neutral) assumption, evolve respectively according to the electron density equation

$$\frac{\partial n}{\partial t} - \frac{c}{B} \nabla\psi \times \hat{\underline{z}} \cdot \nabla n = - \frac{\partial}{\partial z}\left(\frac{en}{m_{-} \nu_{-}} \frac{\partial\psi}{\partial z}\right) \quad (1)$$

and the ion density equation.

$$\frac{\partial n}{\partial t} - \frac{c}{B} \nabla\psi \times \hat{\underline{z}}\cdot\nabla n = \frac{-1}{e}\left[\underline{E}_o - \nabla\psi - \frac{\nu}{\omega_c}(\underline{E}_o - \nabla\psi)\times\hat{\underline{z}}\right]\cdot\nabla\sigma_p$$

$$+ \frac{\sigma_p}{e}\nabla^2\psi + 2\frac{T}{e^2}\nabla^2\sigma_p \quad (2)$$

where $\hat{\underline{z}} = \underline{B}/|B|$, ν denotes collision frequency, ω_c denotes cyclotron frequency, e is the electronic charge (positive), T, is temperature in energy units, the minus subscript denotes electron quantities (so that ν appearing alone will mean ion collision frequency and similarly for ω_c), σ_p is the Pedersen conductivity taken as

$$\sigma_p = \frac{nec}{B} \frac{(\nu/\omega_c)}{1+(\nu/\omega_c)^2}$$

and ψ is related to the ordinary induced electrostatic potential ϕ by

$$\nabla\psi = \nabla\phi - \frac{T}{e}\frac{1}{n}\nabla n \tag{3}$$

Equations (1) and (2) are readily derivable from Eqs. (3) and (4) of Goldman et al., [1974] and are in the $\underline{E}_o \times \underline{B}$ drift frame.

We view the striations as due to the first order variation in a zero order background. On expanding Eqs. (1) and (2) with

$$\nabla\psi = \nabla\psi_o + \nabla\psi_1 \tag{4}$$

$$n = n_o + n_1 \tag{5}$$

we obtain

$$\frac{\partial n_o}{\partial t} - \frac{c}{B}\nabla\psi_o \times \hat{\underline{z}} \cdot \nabla n_o = -\frac{\partial}{\partial z}\left(\frac{\sigma_{\|o}}{e} \frac{\partial\psi_o}{\partial z}\right) \tag{6}$$

$$\frac{\partial n_o}{\partial t} - \frac{c}{B} \nabla\psi_o \times \underline{\hat{z}} \cdot \nabla n_o = - \frac{1}{e} \left[\underline{E}_o - \nabla\psi_o - \frac{\nu}{\omega_c} (\underline{E}_o - \nabla\psi_o) \times \underline{\hat{z}} \right] \cdot \nabla\sigma_{po}$$

$$+ \frac{\sigma_{po}}{e} \nabla^2\psi_o + \frac{2T}{e^2} \nabla^2\sigma_{po} \tag{7}$$

and for the first order terms

$$\frac{\partial n_1}{\partial t} - \frac{c}{B} \left[\nabla\psi_o \times \underline{\hat{z}} \cdot \nabla n_1 + \nabla\psi_1 \times \underline{\hat{z}} \cdot \nabla n_o \right]$$

$$= - \frac{\partial}{\partial z} \left[\frac{\sigma_{||o}}{e} \frac{\partial\psi_1}{\partial z} + \frac{\sigma_{||1}}{e} \frac{\partial\psi_o}{\partial z} \right] \tag{8}$$

$$\frac{\partial n_1}{\partial t} - \frac{c}{B} \left[\nabla\psi_o \times \underline{\hat{z}} \cdot \nabla n_1 + \nabla\psi_1 \times \underline{\hat{z}} \cdot \nabla n_o \right]$$

$$= - \frac{1}{e} \left[\underline{E}_o - \nabla\psi_o - \frac{\nu}{\omega_c} (\underline{E}_o - \nabla\psi_o) \times \underline{\hat{z}} \right] \cdot \nabla\sigma_{p1}$$

$$+ \frac{1}{e} (\nabla\psi_1 - \frac{\nu}{\omega_c} \nabla\psi_1 \times \underline{\hat{z}}) \cdot \nabla\sigma_{po} + \frac{\sigma_{p1}}{e} \nabla^2\psi_o$$

$$+ \frac{\sigma_{po}}{e} \nabla^2\psi_1 + \frac{2T}{e^2} \nabla^2\sigma_{p1} \tag{9}$$

where we have used $\sigma_{||} = ne^2/m_-\nu_-$.

We neglect any altitude variation within the barium cloud and assume that the striations are localized in a region perpendicular to $\underline{B}$ with barium density given by $n_{bo}(x)$. Further we assume

$\underline{E}_o - \nabla\psi_o = \underline{E}(x)$. The assumption $\partial\underline{E}/\partial y = 0$ is necessary for harmonic variation in the y direction. The assumption $\partial\underline{E}/\partial z = 0$ is based on $\partial\psi_o/\partial z = 0$, which is reasonable for striations with variation exp [iky] such that $k L_\perp \gg 1$ where $L_\perp = |\partial \ln n_{bo}/\partial x|^{-1}$. That is, we expect that the zero-order potential associated with $L_\perp$ is essentially constant in z over distances for which the first order striation potential, associated with a more rapid variation perpendicular to $\underline{B}$, is varying. The background ionospheric density is taken to depend only on z and represents an extension over the work of Völk and Haerendel [1971] and Perkins et al. [1973] who assumed a constant background ionosphere. This neglects any zeroth order image clouds in the background ionosphere (see Goldman et al., 1974; and Scannapieco et al., 1974) and is certainly true at early times in the barium cloud development. It is also interesting to note that neglect of density gradients perpendicular to $\underline{B}$ in the background ionosphere appears reasonable for the inhomogeneous steady state consistent with our assumptions (see appendix A for discussion). The zero-order background may in principle be varying in time; since the striation growth rate at any given time depends only on the zero-order parameters at the same time, this effect will be neglected.

With the preceding discussion in mind we take

$$\nabla\psi = [\nabla\psi_o](x) + \nabla[\psi_1(z)e^{iky+\gamma t}] \tag{10}$$

and

$$n = n_o(x,z) + n_1(z)e^{iky+\gamma t} \tag{11}$$

By omitting the x variation in first order quantities we overestimate γ by a fraction proportional to $(kL_\perp)^{-1}$ due to nonlocalization of the mode [Goldman, 1971] and neglect the modification of the instability by current along the density gradient [Perkins and Doles, 1975]. The latter effect, according to the authors, can (at least in the absence of diffusion) vanish completely with appropriate direction of the electric field for the case of two-dimensional striation variation transverse to the magnetic field.

Upon substituting Eqs. (10) and (11) in (8) and (9), going to a reference frame moving with $\underline{v} = -c\,\nabla\psi_o \times \hat{\underline{z}}/B$, using $kL_\perp > 1$ and equivalently $\nabla^2\psi_o < kE$ (valid for $|\nabla\psi_o|/|E| \leq 1$), and expressing n_1 in terms of ψ_1 (through Eq. (9)) as

$$n_1 = \psi_1 n_o \frac{\left[\dfrac{ik\dfrac{c}{B}\dfrac{1}{L_\perp}}{1+\left(\dfrac{\nu}{\omega_c}\right)^2} - k^2\dfrac{c}{B}\dfrac{\nu/\omega_c}{1+\left(\dfrac{\nu}{\omega_c}\right)^2}\right]}{\gamma + \dfrac{\nu/\omega_c}{1+\left(\dfrac{\nu}{\omega_c}\right)^2}\dfrac{c}{B}\left(ik\mathcal{E} + \dfrac{2T}{e}k^2\right)} \tag{12}$$

with $\mathcal{E} = \underline{E}\cdot\hat{\underline{y}} + (\nu/\omega_c)\underline{E}\cdot\hat{\underline{x}}$ ($\hat{\underline{x}}$ and $\hat{\underline{y}}$ are unit vectors in the x and y directions, respectively), we finally obtain

$$\Gamma \psi_1 - \frac{\partial}{\partial z}\left(\sigma_{\|o} \frac{\partial \psi_1}{\partial z}\right) = 0 \tag{13}$$

where

$$\Gamma = k^2 \sigma_{po} \frac{\left[\gamma_1(z)\left(1 + \frac{i\nu_b}{\omega_{cb} k L_\perp} \delta_b\right) + \delta_b\right]}{\left[\gamma_1 - \frac{ikL_\perp \nu/\omega_c}{1 + \left(\frac{\nu}{\omega_c}\right)^2}\right]} \tag{14}$$

In Eq. (14) we have that $\delta_b = 1$ for $z_o \leq z \leq z_1$, where z_o is the bottom of the barium cloud and z_1 is the top of the barium cloud (i.e., within the barium cloud) and $\delta_b = 0$ otherwise (note that the subscript b refers to barium) and also

$$\gamma_1(z) = \frac{\gamma}{\frac{c}{BkL_\perp}\left(-k\mathcal{E} + 2i\,\frac{T(z)k^2}{e}\right)} \equiv \gamma_{1r} + i\gamma_{1i} \tag{15}$$

At this juncture we should point out that Eqs. (13) and (14) outside the barium cloud, i.e., $\delta_b = 0$ reduce to the equation studied by Farley [1959, 1960] and Spreiter and Briggs [1961] if we neglect the factor $-ikL_\perp(\nu/\omega_c)/(1+(\nu/\omega_c)^2)$ in the denominator of Eq. (14). This term arises from the contribution of image density transport in Eq. (9), i.e., in determining the relation between n_1 and ψ_1 for the ionospheric plasma and including effects due to n_1 (essentially the terms involving σ_{p1} on the RHS of Eq. (9)).

Equivalently, if we neglect the $n_1\mathcal{E}$ type contributions to the current in the divergence of the current equal zero equation, then we get the results of Farley [1950, 1960] and Spreiter and Briggs [1961]. That is to say, we have from Eq. (13), in the ionosphere,

$$\nabla_\perp \cdot \underline{j}_{\perp 1} = \Gamma \psi_1 \tag{16}$$

where

$$\Gamma = \frac{k^2 \sigma_{po}^{\,i} \gamma_1}{\gamma_1 - \dfrac{ikL_\perp \nu_i/\omega_{ci}}{1 + (\nu_i/\omega_{ci})^2}} \tag{17}$$

and we have taken the perturbed current as

$$\underline{j}_{\perp 1} = (\underline{E}_\perp - \frac{\nu_i}{\omega_{ci}} \underline{E}_\perp x\hat{\underline{z}})\sigma_{p1}^{\,i} - \frac{2T}{e}(\nabla_\perp \sigma_{p1}^{\,i} + \frac{\omega_{ci}}{\nu_i} \nabla_\perp \sigma_{p1}^{\,i} x\hat{\underline{z}})$$

$$- \sigma_{po}^{\,i}(\nabla_\perp \psi_1 - \frac{\nu_i}{\omega_{ci}} \nabla_\perp \psi_1 x\hat{\underline{z}}) \tag{18}$$

and $\nabla_\perp \sigma_{p1}^{\,i} = ik\hat{\underline{y}}\, \sigma_{p1}^{\,i}$, etc. However, for

$$\underline{j}_{\perp 1} = - \sigma_{po}^{\,i}(\nabla_\perp \psi_1 - \frac{\nu_i}{\omega_{ci}} \nabla_\perp \psi_1 x\hat{\underline{z}}) \tag{19}$$

i.e., only contributions from the perturbed potential ψ_1, we have Eq.(16), but here

$$\Gamma = k^2 \sigma_{po}^{i} \tag{20}$$

Equations (13) and (14) outside the barium cloud are equivalent to equations (61) and (62) of Perkins et al. [1973] if we assume $\nu/\omega_c \ll 1$ and is independent of altitude and noting that we have no x variation for n_1 and ψ_1. Finally Eqs. (13) and (14), in the background ionosphere, are equivalent to Eq. (59) of Völk and Haerendel [1971] if we assume $kL\nu/\omega_c\gamma_1 \ll 1$ and we take a homogeneous ionosphere.

III. Numerical Results and Discussion

On defining

$$K = \sigma_{||o} \frac{\partial \psi_1}{\partial z} \tag{21}$$

we can rewrite Eq. (13) as

$$\frac{\partial^2 K}{\partial z^2} - \frac{1}{\Gamma} \frac{\partial \Gamma}{\partial z} \frac{\partial K}{\partial z} - \frac{\Gamma}{\sigma_{||o}} K = 0 \tag{22}$$

Equation (22) is solved numerically for the case of a barium cloud centered at an altitude of 200 km and assumed to extend from 190 km (z_o) to 210 km (z_1), with $L_\perp = 1$ km, in an ionosphere defined for $z \geq 100$ km. Parameters for the ionosphere are basically those given by Hanson [1961] for nighttime sunspot minimum and maximum (see

Figs. 1-3; note: that the curve in Hanson [1961] for nighttime sunspot minimum for the Pedersen conductivity is in error below the E region peak and in any case our Figs. 1-3 are consistently based on the curves for n_o and ν given by Hanson [1961] and show the ambient ionosphere that we used) and we take the ionospheric temperature, T, in our equationsto be constant so that $\partial \gamma_1 / \partial z = 0$ (see Eq. (15)). {The variation in γ_1, due to the z dependence of $\mathcal{E}$ (through the term $\nu E_x / \omega_c$) is only significant for $\frac{\nu}{\omega_c} \left(\frac{\nu_b}{\omega_{cb}} + \frac{2T}{eE_y L_\perp} \right) \gtrsim 1$, [see Eq. (A-4)], i.e. for $z \approx 100$ km where the Pedersen conductivity is already small; hence it will be neglected.}

The variable K represents the downward current parallel to the magnetic field lines due to the striations. Below about 110 km there is a sharp fall-off in the Pedersen conductivity (see Fig. 1); hence, it appears reasonable to terminate the ionosphere at 100 km. We assume no current flow outside of the ionosphere; therefore $K(\infty) = K(100 \text{ km}) = 0$. The condition $K(\infty) = 0$ coupled with estimates of potential variation for the ionosphere based on decreasing values for the electron-neutral and ion-neutral collision frequencies at high altitudes suggest that we treat the region above the barium cloud as being at constant (unit) potential, i.e., $\psi_1(z) = 1$ for $z \geq 190$ km(z_o). This assumption is investigated numerically as concerns its effects on growth rates and modal structures (see cases IV and V in this section).

The boundary conditions on Eq. (13) may be written as

$$K(z_o) = -\int_{z_o}^{\infty} \Gamma(z')dz' \tag{23a}$$

$$K(100 \text{ km}) = 0 \tag{23b}$$

$$\frac{\partial K}{\partial z}(z_o) = \Gamma(z_o) \tag{23c}$$

(remembering that $z_o = 190$ km) where (23a) and (23b) are the current conditions at infinity and 100 km, respectively and (23c) shows that the potential is taken to be unity at 190 km. Since Eq. (22) is second order and there are three boundary conditions, it is clear that Eqs. (22) and (23) pose an eigenvalue problem. This problem has been solved using the BODEL program (see Appendix B) with 129 points in the range 100 km $\leq z \leq$ 190 km.

Results for perturbed potential, number density, and parallel velocity (all as a function of altitude) and growth rates for wavelengths from 0.2 km to 1.0 km (in steps of 0.1 km) and for wavelengths from 1 km to 6 km (in steps of 1 km) are available for the models listed below. Figures 4-16 display these results for selected wavelengths and different models. The models used, hereafter to be referred to by their Roman numerals, are : (I) the canonical situation of nighttime solarmin (sunspot minimum) conditions [according to Hanson, 1961], a cloud with ratio of height integrated Pedersen

conductivity to that of the background ionosphere, $\Sigma_p^{\ b}/\Sigma_p^{\ i}$, equal to 4 and full coupling to the F region ($\psi_1(z) = 1$, $z > 190$ km); (II) the canonical situation but with $\Sigma_p^{\ b}/\Sigma_p^{\ i} = 0.2$; (III) the canonical situation but with the value zero substituted for $- ikL_\perp \nu/\omega_c/(1+(\nu/\omega_c)^2)$ in the denominator of Eq. (14), so that this effectively suppresses the contribution of image density transport in determining the relationship between n_1 and ψ_1 for the ionospheric plasma and provides the limit, for the ionosphere, appropriate to the earlier calculations of potential variation along field lines [Farley, 1959, 1960; Spreiter and Briggs, 1961; and Swift, 1972]; (IV) the canonical situation but with solarmax conditions [Hanson, 1961]; and (V) the same situation as (IV) but with the assumption $\psi_1(z) = 1$ for 190 km $< z < 210$ km and $\psi_1(z) = 0$ for $z > 210$ km. The difference between (IV) and (V) is presented to provide an upper bound on the uncertainty due to F region coupling. It is worthwhile to point out at this juncture that for solarmin, from Fig. 1, that $\Sigma_p^{\ i} = 0.19$ mhos while $\Sigma_p^{\ i}$ (above the barium cloud) $= 0.04$ mhos; whereas, for solarmax $\Sigma_p^{\ i} = 0.73$ mhos while $\Sigma_p^{\ i}$ (above cloud) $= 0.58$ mhos.

Eigenmodes. ψ_1 is normalized so that $\psi_1(190) = 1$; whereas n_1 and K are presented in units of $(k\psi_1/\mathcal{E})$. For $\Sigma_p^b/\Sigma_p^i \gg 1$ one expects $k\psi_1/\mathcal{E} \sim 1$, and for $\Sigma_p^b/\Sigma_p^i \ll 1$ one expects $k\psi_1/\mathcal{E} \sim (\Sigma_p^b/\Sigma_p^i)^{\frac{1}{2}}$, before non-linear effects on modal structure set in.

The phase variation present in all cases except III (see Figs. 10-14) has the following interpretation: A modal structure

for ψ_1 (or $v_{1z} \equiv \frac{K}{N_o e}$ or n_1) can be written as

$$(\psi_{1_r} + i\,\psi_{1_i}) \exp\,(iky + \gamma t)$$

or equivalently as

$$|\psi_1| \exp[iky + i\xi(z) + \gamma t]$$

with $|\psi_1| = \sqrt{\psi_{1r}^{\,2} + \psi_{1i}^{\,2}}$ and $\sin\xi(z) = \psi_{1i}/|\psi_1|$, $\cos\xi(z) = \psi_{1r}/|\psi_1|$. Hence the phase $\left\{\equiv [ky + \xi(z) + \gamma_i t]\right\}$ is the same at a given time for locations $y(190^-)$ and $y(z)$, just below 190 km and at z, respectively, provided:

$$y(z) = y(190^-) + \frac{[\xi(190^-) - \xi(z)]}{2\pi}\lambda + m\lambda$$

where m is integral or zero and $\lambda = 2\pi/k$ is the wavelength perpendicular to the magnetic field in the y direction; i.e. the harmonic modal structures shift along the y-axis as z varies. This variation is shown for case I at .8 km in Fig. (4a) and for case II at .4 km in Fig. (4b). (The shifts are reflected around y = o for a negative $\underline{B}$ field as is appropriate for the northern hemisphere.) It is interesting to point out that in both cases presented in Fig. 4 the density variation, n_1, just under the cloud (190 km) is out of phase with the striations in the cloud by approximately 90° (1/4 of a wavelength).

This is in agreement with the homogeneous ionosphere theory given by Völk and Haerendel [1971]. However, the subsequent density variation, as one descends in altitude, is not as pronounced nor amenable to as simple an interpretation as given by their Fig. 8 (or the text pertaining to that figure), i.e., real ionospheres are somewhat more complicated than homogeneous ionospheres in the treatment of the image problem.

One notes that one may define a wave-vector

$$k_z(z) \equiv k_{zr}(z) + ik_{zi}(z)$$

such that

$$k_{zr}(z) = d\xi(z)/dz$$

and

$$k_{zi}(z) = - d \ln|\psi_1(z)|/dz$$

to characterize the z-variation of ψ_1 (or v_{1z} or n_1). With a spatially homogeneous ionosphere, $dk_z/dz \equiv 0$ (see for example Völk and Haerendel, 1971) and so one has k_{zr} and k_{zi} being constant as a function of altitude (although not equal). In our study k_{zr} and k_{zi} are functions of altitude and in general are not simple (this can be seen by examining Figs. 5-14).

For Case I the potential is progressively less localized with increasing wavelength (see Fig. 5a). At all wavelengths there is an imaginary component to the potential (see Fig. 10a); at relatively shorter wavelengths this component, which can dominate over the real component of the potential at the same altitude, can be as large as 0.3 of the value of the potential at 190 km. The values for $v_{1z}(190)$ which are typically 3.5×10^5 cm/sec for $k\psi_1/\mathcal{E} = 1$, are closely spaced for $\lambda \leqslant 1.0$ km and decrease in magnitude as λ increases above 1.0 km (see Fig. 5b) The imaginary components of $v_{1z}(190)$ are roughly 2/3 of the real components of $v_{1z}(190)$ (see Fig. 10b). It can be shown that

$$\frac{K}{k^2}(\psi_1 = 1) = \frac{n_o e v_{1z}}{k\mathcal{E}} (k\psi_1(190)/\mathcal{E} = 1) \qquad (24)$$

where $K(\psi_1 = 1)$ is the value of K appropriate to $\psi_1(190) = 1$ and $v_{1z}(k\psi_1(190)/\mathcal{E} = 1)$ is the value of v_{1z} appropriate to $k\psi_1(190)/\mathcal{E} = 1$, i.e. the value of v_{1z} plotted in our figures. Since the contribution of the region below the barium cloud to γ_1 occurs solely through $K(\psi_1 = 1)$, see Eq. (28), one sees that one can parametrize the entire region below the barium cloud by an effective complex Pedersen conductivity, $\tilde{\Sigma} \left(\equiv \frac{K_r}{k^2} + i\,\frac{K_i}{k^2}\right)$, which varies roughly as k^{-1} for $\lambda \leq 1.0$ km. By Eq. (24) the plots of v_{1z}, particularly $v_{1z}(190)$, directly yield the values of $\tilde{\Sigma}$, and the locations of the digits, m, $m < 0$ give effective integrated conductivities between 100 km and

the location denoted by (100 + 10 m) km. The values for n_1, expressed analytically in terms of ψ_1 by Eq. (12), show that the imaging for relatively long wavelength disturbances peaks at the Pedersen conductivity maximum, between z = 120 and z = 130 km, but that the imaging from shorter wavelengths peaks at higher altitudes and is slightly weaker (see Figs. 5c and 10c).

The results from case II for the potential, ψ_1, are strikingly less localized than those from case I (see Figs. 6a and 11a). This is consistent with the lower value of $|\gamma_1|$ (see Fig. 15) which leads to decreased values of $\nabla_\perp \cdot \underline{j}_{\perp 1}/\psi_1$ and hence [through Eq. (13)] to larger scale lengths for the variation of ψ_1 in the z-direction, as well as the relatively larger size of $\gamma_{1i}/|\gamma_1|$ for Case II [see Eqs. (24a) and (24b) and subsequent discussion]. The behavior at .2 km for Case II is particularly interesting in view of the non-monotonicity of ψ_1. Such a result is possible with Eq. (13) if there exist values of z where $\beta\gamma_{1i} > |\gamma_1|^2$, (with $\beta = kL_\perp\nu/[\omega_c(1 + \nu^2/\omega_c{}^2)]$). To see this we note on multiplying Eq. (13) by ψ_1^*, integrating between 100 km and z, using $\sigma_{||o}\partial\psi_1/\partial z(100) = 0$, performing the analogous operations on the complex conjugate of Eq. (13) and adding the results that one obtains:

$$\int_{100}^{z} (\Gamma + \Gamma^*)\psi_1\psi_1{}^* dz' + 2\int_{100}^{z} \sigma_{||o} \frac{\partial\psi_1}{\partial z}\frac{\partial\psi_1{}^*}{\partial z} dz'$$

$$= \sigma_{||o} \frac{\partial}{\partial z} |\psi_1|^2 \quad , \qquad (24a)$$

where for $z < z_o$:

$$(\Gamma + \Gamma^*)/k^2\sigma_{po} = \frac{2|\gamma_1|^2 - 2\gamma_{1i}\beta}{|\gamma_1|^2 + \beta^2 - 2\gamma_{1i}\beta} \tag{24b}$$

In the zero temperature limit when the left hand side of (24a) is equal to $\mathrm{Re}\ 2\int_{z=100}^{z} \underline{j}_1 \cdot \underline{E}_1 dz'$ the condition $\sigma_{||o}\partial|\psi_1|^2/\partial z < 0$ corresponds to the existence of a physical volume $100 \leq z' \leq z$ within which the ionospheric particles do work on the wave rather than the opposite. On the other hand if one neglects the contribution in β to Γ from (24a) and (24b) one has the more usual result:

$$\sigma_{||o}\ \partial|\psi_1|^2/\partial z > 0 \quad .$$

Further one notes through (24a) and (24b) the possibility of connection between $\gamma_{1i}\beta > |\gamma_1|^2$ and decreased values for $|\partial\psi_1/\partial z|$ and $\partial|\psi_1|^2/\partial z$, and hence the possibility of less localization of the potential with $\gamma_{1i} > 0$, even if $\partial|\psi_1|^2/\partial z > 0$ for all $z(< z_o)$.

The behavior for v_{1z} (and hence $\tilde{\Sigma}$) is markedly different from that of Case I. $|v_{1z}(190)|$ is monotonically decreasing as a function of increasing wavelength (see Fig. 6b); further the real part of $v_{1z}(190)$ is relatively constant, whereas the imaginary part of $v_{1z}(190)$ decreases with increasing wavelength (see Fig. 11b). This corresponds to a picture of $\tilde{\Sigma}$ whose real part varies roughly as k^{-1} but whose imaginary part is roughly constant at short wavelengths and at any rate varies less rapidly with k. In keeping with the non-linear results for barium clouds with $\Sigma_p^b/\Sigma_p^i = \epsilon << 1$ [Goldman et al.,

1974] we would expect the maximum attainable velocities in the linear regime to be multiplied by a factor less than unity. (For $\epsilon \ll 1$, this factor would be $\sim \epsilon^{1/2}$.) The densities are less sharply peaked than those for Case I and larger in terms of $(k\psi_1/\mathcal{E})$ especially at short wavelengths.

The modal structure curves for ψ_1, v_{1z} and n_1 of Case III (see Fig. 7) are universal in the sense that they are independent of γ_1 (or equivalent of the ratio $\Sigma_p^{\,b}/\Sigma_p^{\,i}$.) Hence Case III can be directly compared with both Cases I and II as concerns modal structure. Agreement is closer between Cases III and I than between III and II.

The results from Case III for ψ_1 (see Fig. 7a) are more localized than those from Case I although the values of γ_1 are very close. Comparison of Eqs. (17) and (20) results in the modification of the first term of Eq. (13) by a factor of $\gamma_1/(\gamma_1 - i\beta)$ in passing from Case III to Case I. Hence at wavelengths with $kL_\perp \gg 1$ with locations in z with $\beta \gg |\gamma_1|$, $\partial/\partial z(\sigma_{||o}\partial\psi_1/\partial z)$ is clearly smaller for Case I than for Case III and the potential does not vary as rapidly in z.

The values of $|v_{1z}(190)|$ for Case III (see Fig. 7b) are characteristically 20-30% higher than those for Case I indicating corresponding larger values for $|\tilde{\Sigma}|$ and hence lower growth rates. The constancy of $|v_{1z}(190)|$ for $\lambda \le 1.0$ km indicates that $|\tilde{\Sigma}|$ varies as k^{-1} in this range of λ. The contrast with $\tilde{\Sigma}$ from Case II is striking. The values of $|n_1|$ for Case III (see Fig. 7) are higher in maximum value and more localized in space than those for Case I; $n_1(z)$ bears a fixed phase relation to $\psi_1(z)$, independent of z (see Fig. 12).

The results from Case IV for ψ_1 (see Figs. 8a and 13a) indicate more localization in the vicinity of the barium cloud than for Case I. Mathematically, for two ionospheres, a and b, with neutral densities n such that $n_a(z)/n_b(z) = \alpha$ the modal structure is the same for wavelengths λ_a and λ_b such that $\lambda_a = \alpha\lambda_b$, provided each of the modes is localized in a region with $\nu/\omega_c \ll 1$. Since the neutral densities in the vicinity of the barium cloud are roughly a factor of two larger for solarmaximum than for solarminimum conditions, the rough equivalence for potential variation in the vicinity of the barium cloud for wavelengths such that $\lambda(\text{Case IV})/\lambda(\text{Case I}) \approx 2$ is plausible. At lower altitudes where the ionospheres of Cases I and IV are more similar the fall off in ψ_1 with decreasing z at the same wavelength is closer. This gives the curves of $|\psi_1|$ for Case I a more bowed appearance than those of Case IV.

The values of $|v_{1z}(190)|$ for both cases are similar (see Figs. 5b and 8b). At relatively small values of λ, $v_{1zi}(190)/v_{1zr}(190)$ is larger for Case IV (see Fig. 13b) than for Case I (see Fig. 10b). This effect which also is pronounced for short wavelengths in Case II is apparently related to relatively large values of γ_{1i}, as can be seen from the analytic expression:

$$v_{1z}(190) = \frac{k^2}{n_o(190)e} \int_{100}^{190} \left[\frac{\gamma_{1r}^2 + \gamma_{1i}(\gamma_{1i}-\beta) + i\beta\gamma_{1r}}{\gamma_{1r}^2 + (\gamma_{1i}-\beta)^2} \right] \cdot \tag{25}$$

$$\psi_1(z')\sigma_{po}(z')dz' \quad ,$$

which indicates the possibility of negative contributions to v_{1zr} for regions of space such that $\beta\gamma_{1i} > |\gamma_1|^2$. At short wavelengths the maxima for $|n_1|$ in Case IV (see Fig. 8c) are larger and occur at higher altitudes than in Case I (see Fig. 5c). This corresponds to the larger Pedersen conductivity under solarmaximum conditions at higher altitudes in the range $100 \leq z \leq 190$ as well as the greater localization of ψ_1. At large wavelengths the agreement is closer with the maxima in $|n_1|$ still at slightly higher altitudes.

The results from Case V for ψ_1 (see Figs. 9a and 14a) are very similar to those from Case IV except at short wavelengths where there is more localization of the potential near the barium cloud. At short wavelengths one notes that γ_{1i} from Case IV is relatively much larger than γ_{1i} for Case V (see Fig. 15). By Eqs. (24a) and (24b) this suggests a less rapid decrease of $|\psi_1|$ with increasing distance from the barium cloud. The larger values of $|v_{1z}(190)|$ at short wavelengths in Case IV (see Figs. 8b and 9b) are attributable to the larger magnitudes of $v_{1zi}(190)$ which appear to be due to the large values of ψ_{1i} for $z \geqslant 150$ km. The larger values of n_1 (see Figs. 8c and 9c) at short wavelengths in Case IV are attributable to the less rapid fall-off in ψ_1 away from $z = 190$ as well as the more negative values of the imaginary part of γ.

Coupling above the barium cloud and eigenvalues. In this section, we first present conclusions obtained in Appendix D regarding electrostatic coupling above the barium cloud. We then apply these notions to the estimation of induced velocities parallel to the magnetic field,

density inhomogeneities, and the calculation of eigenvalues taking partial coupling to the F region conductivity maximum into account. The reader is referred to Appendix D for analytic details.

For $z > z_1$, the treatment of Appendix D indicates for $\lambda \geq 0.2$ km and the barium clouds of Cases I and II, or for $\lambda \geq 0.5$ km and the barium clouds of Cases IV and V, that the dominant part of $\psi_1(z)$ is given by

$$\psi_{1O}(z) \approx \frac{1 + \alpha(z)}{1 + \alpha(z_1)} \psi_1(z_1) \tag{26}$$

This result is in close agreement with the physical model in which $\psi_{1\infty}$, the potential [assumed constant and equal to $\psi_1(\infty)$] at the F region conductivity peak $(z > z^*)$, causes an integrated horizontal current divergence $-\int_{z^*}^{\infty} \Gamma\psi_{1\infty} dz$ for $z^* \leq z \leq \infty$ which in turn draws a vertical current $-\int_{z^*}^{\infty} \Gamma\psi_{1\infty}\, dz$ into the region $z > z^*$ along the magnetic field lines. If there is no significant perpendicular shorting of current between z_1 and z^*, so that:

$$\int_z^{\infty} \Gamma\psi_1 dz' \approx \int_z^{\infty} \Gamma\psi_{1\infty} dz' \approx \int_{z^*}^{\infty} \Gamma\psi_{1\infty}\, dz'$$

one has:

$$-\sigma_{\|o} \frac{d\psi_1}{dz} \approx -\int_z^{\infty} \Gamma\psi_{1\infty} dz',$$

from which (26) follows, provided one takes $kL_{\perp}\nu/\omega_c \ll 1$ for $z > z_1$.

For Cases I and II, we have $\alpha(z_1) = 3.2 \times 10^{-2}\lambda^{-2}$, and for Cases IV and V, $\alpha(z_1) = \lambda^{-2}$, where λ is in km. Further we note $\alpha(z) < \alpha(z_1)$ for $z > z_1$, so that $d\psi_{10}/dz < 0$, $z > z_1$. For the F region conductivity peak region [$z > z^*$ (= 280 km at solarmax), $z > z^*$(= 270 km at solarmin), see Fig. 1], we have $\alpha(z) \leq 0.2$. Hence for solarmin conditions a transition from little coupling to the F region conductivity maximum to full coupling is indicated as λ increases through 0.2 km; while for solarmax conditions the transition is indicated for λ = 1.0 km.

In analogy to Eq. (25) one has on neglect of contributions in β which are expected to be small by virtue of the discussion of Appendix D:

$$v_{1z}(z_1) = - \frac{k^2}{en_o(z_1)} \int_{z_1}^{\infty} \sigma_{po}\psi_1(z')dz' , \tag{27a}$$

which by (28'. and (28''), q.v., yields [with $k\psi_1(z_1) = \mathcal{E}$]:

$$v_{1z}(z_1) = - \frac{k\mathcal{E}\int_{z_1}^{\infty} \sigma_{po}dz'}{en_o(z_1)\,[1 + \alpha(z_1)]} \tag{27b}$$

Within the range of validity of Appendix D under solarmin conditions, the maximum value for $v_{1z}(z_1)$, z_1 = 210, occurs for λ = 0.2 km where $v_{1z}(z_1) = 5 \times 10^5$ cm/sec; under solarmax conditions the maximum value occurs for λ = 1.0 km where $v_{1z}(z_1) = 1.4 \times 10^6$ cm/sec.

From Eq. (12) on neglecting terms of order $kL_\perp \nu/\omega_c$ in the denominator, one has that

$$n_1(z) \approx - k^2\sigma_{po}\psi_1(z)/e\gamma. \tag{27c}$$

For all cases covered by Eq. (26), $n_1(z)$ is largest in magnitude for $z > z^*$. On using $\gamma = \tilde{\gamma}\, c\mathcal{E}/BL_\perp$ with $\tilde{\gamma}$ of order unity, Eq. (27c) leads to the result

$$\frac{n_1(z)}{n_o} = \frac{-[1 + \alpha(z)]}{[1 + \alpha(z_1)]} \; \frac{k\psi_1(z_1)}{\mathcal{E}\tilde{\gamma}} \; kL_\perp \frac{\nu}{\omega_c} \tag{27d}$$

Hence for striations with $k\psi_1(z_1)/\mathcal{E}\tilde{\gamma} \approx 1$, as is expected to be the case at the limit of a linear treatment, $n_1(z)/n_o$ can be as large as 3×10^{-2}, (at $\lambda \approx 1$ km and $z \approx 300$ km. under solarmax conditions,or at $\lambda \approx 0.2$ km and $z \approx 280$ km under solarmin conditions.)

First, as concerns eigenvalues, it is interesting to note that the eigenvalue agreement between Cases III and I (see Fig. 15) is considerably closer than between Case III$'$ ($\Sigma_p^b/\Sigma_p^i = 0.2$, but neglect of image density transport) and Case II (see Fig. 15a). In comparing these cases (in Fig. 15a and remembering that III and III$'$ neglect the effect of images back on striation growth, i.e., no image transport) we do not find, for a real ionosphere, the pronounced effect of image striations reducing the growth rate that Völk and Haerendel [1971] found for the homogeneous ionosphere (see their Fig. 9). For Case IV (full coupling to the F region), as depicted in Fig. 15a, for long wavelengths $-\gamma_{1r} = 0.8$ which represents the short-circuited

growth rate since $\Sigma_p^{\ b}/\Sigma_p^{\ i} = 4.0$. For Case V, (no coupling to the F region) Fig. 15a shows that for long wavelengths $-\gamma_{1r} \approx 0.95$. This can be understood by the fact that although we chose $\Sigma_p^{\ b}/\Sigma_p^{\ i} = 4.0$ in this case, there is no coupling to the F region where most (~ 80%) of the integrated conductivity occurs (recall that for solarmax $\Sigma_p^{\ i} = 0.73$ mhos, and $\Sigma_p^{\ i}$ (above cloud) = 0.58 mhos). Consequently, the effective integrated conductivity of the ionosphere for long wavelengths is 0.15 mhos so that effectively $\Sigma_p^{\ i}/\Sigma_p^{\ b} \approx 0.05$ and this results in a short-circuited value of 0.95 for $-\gamma_{1r}$.

To obtain modifications on γ_1 and γ due to partial coupling to the F region, we note that Eq. (13) yields, on integrating upwards to "∞" from z_o, the bottom of the barium cloud, using Eq. (21) and neglecting $\delta_b \nu_b/\omega_{cb} kL_\perp$

$$\frac{\Sigma_p^{\ b}(\gamma_1 + 1)}{\gamma_1 - \dfrac{ikL_\perp \nu_b/\omega_{cb}}{1 + \nu_b^{\ 2}/\omega^2_{cb}}} + \int_{z_o}^{\infty} \frac{\sigma_{po}\gamma_1\psi_1(z')dz'}{\gamma_1 - \dfrac{ikL_\perp \nu/\omega_c}{1 + \nu^2/\omega_c^{\ 2}}} + \frac{K_r'}{k^2} + \frac{iK_i}{k^2} = 0, \quad , \qquad (28)$$

with $K(k,z_o) \equiv K_r + iK_i$ and $\psi_1(z_o) = 1$. From Eq. (26) and the discussion after Eq. (D-14b) one sees that the bulk of the contribution to the integral of Eq. (28) comes from the region with $z > z^*$ where $kL_\perp\ \nu/[\omega_c(1 + \nu^2/\omega_c^{\ 2})] \ll \gamma_1$ and $\psi_1(z') \approx \psi_{1o}(\infty) \approx 1/[1 + \alpha(z_1)]$. Hence the integral may be approximated by

$$\int_{z^*}^{\infty} \sigma_{po}\psi_{10}(\infty)\, dz' \qquad (28')$$

which in turn may be approximated by $\Sigma_p^{\ f}/[1 + \alpha(z_1)]$ where

$$\Sigma_p^{\ f} \equiv \int_{z_o}^{\infty} \sigma_{po}^{\ i}\, dz'. \qquad (28'')$$

Then Eq. (28) yields

$$\gamma_1 = -\frac{\left\{ \Sigma_p^{\ b}[\Sigma_p^{\ b} + \Sigma_{pr}^{\ i}(k)] + \frac{kL_\perp}{(1 + \nu_b^{\ 2}/\omega_{cb}^{2})} \frac{\nu_b}{\omega_{cb}} \Sigma_{pi}^{\ i}(k)\Sigma_p^{\ b} \right\}}{\Delta} \qquad (29)$$

$$+i\,\frac{\left(\Sigma_p^{\ b}\Sigma_{pi}^{\ i}(k) + \frac{kL_\perp}{(1 + \nu_b^{\ 2}/\omega_{cb}^{2})} \frac{\nu_b}{\omega_{cb}} \left\{ \Sigma_{pr}^{\ i}(k)[\Sigma_p^{\ b} + \Sigma_{pr}^{\ i}(k)] + [\Sigma_{pi}^{\ i}(k)]^2 \right\}\right)}{\Delta}$$

where $\Delta = [\Sigma_p^{\ b} + \Sigma_{pr}^{\ i}(k)]^2 + [\Sigma_{pi}^{\ i}(k)]^2$,

$\Sigma_{pr}^{\ i}(k) = K_r/k^2 + \Sigma_p^{\ f}/[1 + \alpha(z_1)]$, and

$\Sigma_{pi}^{\ i}(k) = K_i/k^2$. Eq. (29) and the resulting values of γ have been evaluated using values for K_r and K_i obtained from Cases I, II and IV. We note from Eq. (24) that the values of $\frac{K_r}{k^2}$ and $\frac{K_i}{k^2}$ are directly

related to v_{1z}, evaluated at z = 190 km; further that v_{1z} evaluated at 190 km is given in Figs. 10b - 14b.

For either the solarmax or the solarmin case with partial coupling and $\Sigma_p{}^b/\Sigma_p{}^i = 4.0$ we note that both the values of γ_1 and the ionospheres below the barium clouds are similar; further from comparison of Cases IV and V at the same k, one has $|\Delta K|/|K| \approx |\Delta\gamma_1|/|\gamma_1|$. (Here $\Delta\gamma_1$ specifies the variation of an eigenvalue and ΔK is the corresponding variation of K.) In addition we have $\Delta K \approx K'(-1)\Delta\gamma_1$, where $K = K(\gamma_1)$ and $K'(-1) = \partial K/\partial\gamma_1$ evaluated at $\gamma_1 = -1$, so that with $|\gamma_1| \sim 1$, $K'(-1) \sim K(-1)$.

On taking $\Sigma_p{}^b$ large compared to other terms in Eq. (29) as is generally appropriate for $\Sigma_p{}^b/\Sigma_p{}^i = 4.0$, we may write Eq. (29) to lowest order in $(\Sigma_p{}^b)^{-1}$ as:

$$\gamma_1 + 1 = \frac{1}{\Sigma_p{}^b}\left(\left[\frac{K_r}{k^2} + \frac{\Sigma_p{}^f}{1 + \alpha(z_1)} - \frac{kL_\perp}{(1+\nu_b^2/\omega_{cb}^2)}\;\frac{\nu_b}{\omega_{cb}}\;\frac{K_i}{k^2}\right]\right.$$
$$\left. + \, i\left\{\frac{K_i}{k^2} + \frac{kL_\perp}{(1+\nu_b^2/\omega_{cb}^2)}\;\frac{\nu_b}{\omega_{cb}}\left[\frac{K_r}{k^2} + \frac{\Sigma_p{}^f}{1+\alpha(z_1)}\right]\right\}\right), \qquad (29a)$$

with $K = K(\gamma_1) \approx K(-1) + (\gamma_1 + 1)\,K'(-1)$. Since the quantity $(\gamma_1 + 1)$ is small if $\Sigma_p{}^b$ is relatively large, the terms linear in $K'(-1)$, $\sim (\gamma_1 + 1)^2$, are of second order in the smallness parameter, $(\gamma_1 + 1)$. Hence the values of K_r and K_i obtained from full coupling can be used with partial coupling to first order accuracy in $(\gamma_1 + 1)$.

For the solarmax situation, the partial coupling calculations for $\lambda \geq 0.5$ km (see Fig. 16) attach smoothly to the uncoupled calculations of Case V (see Fig. 15) for $\lambda < 0.5$ km. For the solarmin situation the partial coupling results for $\lambda \geq 0.2$ km (see Fig. 16) go smoothly into the full coupling results at about $\lambda = 0.8$ km (see Fig. 15). For both solarmin and solarmax situations one concludes that there is no cut-off in the striation growth rates at short wavelengths due to interactions with the ambient inhomogeneous ionospheric plasma.

For Case II, the eigenvalue estimates are not as reliable since we do not have the data comparable to that of Cases IV and V, and since the ordering in $(\gamma_1 + 1)$ does not obtain. For $\lambda \geq 0.4$ km the eigenvalues with full and partial coupling agree to within 20%, (see Figs. 15 and 16), so that there is presumably little uncertainty in this range. One can obtain an upper bound on growth rates at shorter wavelengths under the assumption that coupling below the barium cloud reduces γ_r. Then choosing $K = 0$ for $\lambda = 0.2$ km with partial F region coupling yields $\gamma_r < 0.23$, which appears sufficient to establish the dip below $\gamma_r \approx 0.30$ at short wavelengths.

In addition, we find, at wavelengths sufficiently short that the perturbations can be regarded as just localized within a (substantially) constant region of the ionosphere, that coupling to the ionosphere yields the growth rate:

$$\gamma_r = \frac{c\mathcal{E}}{BL_\perp}\left(1 - 9.4\,\frac{T}{e\mathcal{E}}\,k\,\frac{\sigma_{po}^{\,i}}{\sigma_{po}^{\,b}}\right) \tag{30}$$

with $k = \sqrt{3}\ \omega_{ci}/L_\perp\ \nu_i$ and $\sigma_{po}^{\ i}$ the approximate local Pedersen conductivity at the level of the barium cloud, provided $\sigma_{po}^{\ i}/\sigma_{po}^{\ b} << 1$, (see Appendix E for details). For solarmax conditions, with $\Sigma_p^{\ b}/\Sigma_p^{\ i} = 4.0$, we obtain $\gamma_r = 0.98\ c\mathcal{E}/BL_\perp$ at $\lambda = 1.1 \times 10^2$m; for solarmin conditions, with $\Sigma_p^{\ b}/\Sigma_p^{\ i} = 4.0$ we obtain $\gamma_r = 0.91\ c\mathcal{E}/BL_\perp$ for $\lambda = 47$m, and with $\Sigma_p^{\ b}/\Sigma_p^{\ i} = 0.2$ we obtain $\gamma_r = -\ 0.9\ c\mathcal{E}/BL_\perp$ at $\lambda = 47$m, where in obtaining the above values we have used $\mathcal{E} = 5$ mV/m and $T = 10^3\ {}^{\circ}K$.

IV. Summary and Conclusions

In this work we have attempted to provide a critical quantitative basis for the study of the structuring and growth rates of striations associated with barium clouds in the ionosphere (i.e., a real ionosphere whose properties vary with altitude). We have been concerned with three zero-order physical situations for a barium cloud between 190 and 210 km ($\Sigma_p^{\ b}/\Sigma_p^{\ i} = 4.0$, solarmin conditions; $\Sigma_p^{\ b}/\Sigma_p^{\ i} = 0.2$, solarmin conditions; $\Sigma_p^{\ b}/\Sigma_p^{\ i} = 4.0$, solarmax conditions) which have resulted in five models (see Section III, Cases I-V) for striation behavior below the barium cloud. These five models with specified behavior above the barium cloud have been investigated numerically as concerns modal structure and growth rates for the region below the barium cloud (Section III). Analytic estimates have then been used to obtain a more precise specification of the real (rather than model) behavior above the barium cloud (Section III, part under eigenvalues). These in turn have been used to provide corrections to the growth rates (Section III, second part) appropriate to the real physical situations approximated by the original models.

Comparison of Cases I (Σ_p^b/Σ_p^i = 4.0, solarmin) and II (Σ_p^b/Σ_p^i = 0.2, solarmin) establishes the dependence of image structure on Σ_p^b/Σ_p^i for a given wavelength. The smaller conductivity cloud produces image striations farther down into the background E region ionosphere (this is in qualitative agreement with the results of image striations in a homogeneous background given by Fig. 9 in Völk and Haerendel, 1971) with a more uniform effective conductivity as a function of wavelength. Comparison of Cases I and II with Case III (the limit of earlier calculations suppressing image density transport; see Farley, 1959, 1960; and Spreiter and Briggs, 1961) shows that striations penetrate further down into the ionosphere than expected on the basis of Case III and that they make an aspect angle with respect to $\underline{B}$ which varies as a function of altitude (variable parallel component of wavenumber.) Comparison of Cases I and IV (Σ_p^b/Σ_p^i = 4.0, solarmax) establishes the relatively slight dependence of E region coupling on the level of solar disturbance. Comparison of Cases IV (totally coupled F region) and V (no coupling to F region) established the relatively slight dependence of E region coupling on F region coupling even under solarmaximum conditions when the F region conductivity is greatest.

Some comments with respect to the extension of the modal structure results to other situations are in order:

1. One expects that penetration below the barium cloud should increase with increasing $L_\perp$. Put another way, imaging with Case III can be viewed as behavior in the limit $L_\perp \to 0$. Hence reducing $L_\perp$ brings results under solarminimum conditions closer to those of Case III.

2. Imaging with very large clouds presumably obtains with $\gamma_{1r} \approx -1$, $\gamma_{1i} \approx 0$. Case V offers the best approximation to this situation. The transition from Case IV to Case V indicates how the limit $\Sigma_p{}^b/\Sigma_p{}^i \gg 1$ is approached.

3. As an extension of the comparison of Cases I and IV, for very large clouds so that $\gamma_{1r} \approx -1$, $\gamma_{1i} \approx 0$, and short wavelengths such that $\psi_1 \approx 0$ for $\nu/\omega_c \ll 1$, changing the cloud altitude so that the neutral density in the vicinity of the cloud is multiplied by a factor of α should result in the same behavior below the barium cloud for a new wavelength equal to the original wavelength multiplied by a factor of α (provided the scale height variation as a function of altitude is neglected.)

4. If all ionized densities are multiplied by a constant factor the results are unchanged (ψ_1, n_1/n_o, v_{1z} and γ are the same) to the extent that Coulomb collisions can be neglected compared to charged particle-neutral collisions.

Analytic treatment for $z \geq z_1$ indicates for $\lambda \geq 0.2$ km and solar-min conditions and for $\lambda \geq 0.5$ km and solarmax conditions that:

a. ψ_1 is predominantly real and decreasing with increasing z,

b. the maximum of v_{1z} is close to, but above z_1,

c. the maximum of n_1 is close to, but above $z = z^*$ (at about 300 km).

The estimate of a value of $v_{1z}(z_1)$ as high as 1.4×10^6 cm/sec is suggestive of the possibility that striations may drive shorter wave-length ion-cyclotron modes [Kindel and Kennel, 1971]. The estimate

of n_1/n_o as high as 3×10^{-2} suggests that striations may drive F region images at $z \approx 300$ km with $n_1 \geq 10^4$ cm^{-3} for $\lambda = 1.0$ km and solarmax conditions. (The highest values for n_1 can be found above the barium cloud because of the large size of n_o in the F region conductivity peak; however under twilight conditions one would expect more pronounced E region effects.)

The eigenvalue analysis with partial coupling to the F region indicates for $\Sigma_p^{\,b}/\Sigma_p^{\,i} = 4.0$ that γ_r is not significantly decreased (if at all) at short wavelengths; on the other hand, for $\Sigma_p^{\,b}/\Sigma_p^{\,i} = 0.2$, with $\lambda \leq 0.2$ km, γ_r (with $T = 10^3$ ^{o}K, $\mathcal{E} = 5$ mV/m) appears at least 20% below its largest values. The absence of a short wavelength cut-off for γ with $\Sigma_p^{\,b}/\Sigma_p^{\,i} = 4.0$ indicates the need for consideration of finite Larmor radius effects and non-linear effects on the spectral structuring. Further, for the same barium cloud at higher altitudes (and hence with lower Pedersen conductivities) diffusion damping effects would tend to be more significant.

For finite temperatures Eq. (29) yields the growth rate:

$$\gamma_r = \frac{c\mathcal{E}}{BL_\perp} \frac{\Sigma_p^{\,b}[\Sigma_p^{\,b} + \Sigma_{pr}^{\,i}(k)]}{\Delta} \tag{31}$$

$$+ \frac{kc}{B}\left[\frac{\nu_b}{\omega_{cb}} \frac{\mathcal{E}}{(1+\nu_b^{\,2}/\omega_{cb}^{\,2})} \frac{-2T}{e\,L_\perp}\right] \frac{\Sigma_p^{\,b}\Sigma_{pi}^{\,i}(k)}{\Delta}$$

$$- \frac{2k^2Tc}{B} \frac{\nu_b/\omega_{cb}}{1+\nu_b^{\,2}/\omega_{cb}^{\,2}} \left\{\frac{\Sigma_{pr}^{\,i}(k)\left[\Sigma_p^{\,b} + \Sigma_{pr}^{\,i}(k)\right] + \left[\Sigma_{pi}^{\,i}(k)\right]^2}{\Delta}\right\}$$

The shaping of the zero temperature spectrum (as a function of k) is generally in agreement with the intuitive picture of more coupling to the ionosphere and hence more damping at larger wavelengths (short circuiting phenomena). Indeed, the term linear in $\mathcal{E}/L_{\perp}$ represents the growth rate for a barium cloud coupled to an ionosphere with complex conductivity $\Sigma_{pr}^{i}(k) + i\,\Sigma_{pi}^{i}(k)$ at the same potential. The slight increase in damping (or decrease in growth) between the finite temperature growth rate, γ_r, compared with the zero temperature growth rate, $-\gamma_{1r}$, at short wavelengths can be attributed to the term linear in k^2T and corresponds to diffusion damping in the y-direction for a barium ion inhomogeneity with stationary electrons and counter-streaming ionospheric ions (see Appendix C for a discussion of this effect.)

Acknowledgments

We wish to thank Dr. D. Book for useful conversations at the beginning of this study. This work was supported by the Defense Nuclear Agency.

Appendix A - Zero-order ionospheric density gradients

In this Appendix, we estimate, within the framework of Eqs. (6) and (7), modifications on the background ionospheric density at various altitudes consistent with the zero-order barium density profile $\sigma_p^b = \sigma_{po}^b(x)$ and $\underline{E} = \underline{E}(x)$. We will assume a steady state for the region. This probably leads to an overestimate in inhomogeneities because from Eq. (A-2), below, the time necessary to establish an inhomogeneity in response to $\sigma_p^b = \sigma_{po}^b(x)$, $\underline{E} = \underline{E}(x)$ varies as $(\nu/\omega_c)^{-1}$ and hence can be very long for the F-region.

Since $\nabla \times \underline{E} = 0$, $\partial(\nabla\psi_o)_y/\partial x = 0$ and $(\nabla\psi_o)_y$ = constant. Hence in the system moving with $\underline{v} = -c(\nabla\psi_o) \times \hat{z}/B$ for the region of interest Eq. (6) and (7) become:

$$\frac{\partial n_o}{\partial t} = - \frac{\partial}{\partial z}\left(\frac{en_o}{m_- \nu_-} \frac{\partial\psi_o}{\partial z}\right). \tag{A-1}$$

$$\frac{\partial n_o}{\partial t} = -\left(E_x - \frac{\nu}{\omega_c} E_y\right) \frac{1}{e} \frac{\partial\sigma_{po}}{\partial x} + \frac{\partial^2\psi_o}{\partial x^2} \frac{\sigma_{po}}{e} + \frac{2T}{e^2} \frac{\partial^2\sigma_{po}}{\partial x^2}. \tag{A-2}$$

Using (A-2) for the steady state at each level yields

$$E_x = \frac{\nu}{\omega_c} E_y - \frac{\sigma_{po}^h}{\sigma_{po}}\left(-E_x^h + \frac{\nu}{\omega_c} E_y\right) + \frac{2T}{e} \frac{1}{\sigma_{po}} \frac{\partial\sigma_{po}}{\partial x} \tag{A-3}$$

and in particular at the barium level one has:

$$E_x = \frac{\nu_b}{\omega_{cb}} E_y - \frac{\sigma_{po}^{bh}}{\sigma_{po}^{b}} \left(-E_x^{h} + \frac{\nu_b}{\omega_{cb}} E_y\right) + \frac{2T}{e} \frac{1}{\sigma_{po}^{b}} \frac{\partial \sigma_{po}^{b}}{\partial x} . \tag{A-3$'$}$$

Here the barium cloud is taken to occupy the region $x > 0$, $E_y > 0$, $\partial\sigma_{po}^{b}/\partial x > 0$, and the superscript h refers to values at $x = 0^-$, i.e., just outside the projection of the barium cloud along magnetic field lines.

In principle we can regard E_x^h, E_y and σ_p^b as known in (A-3$'$) thereby determining E_x and [through (A-3)] $\sigma_p(x,z)$. The case for $E_x^h = 0$ is particularly simple. On restricting considerations to the region $\sigma_{po}^{b} \gg \sigma_{po}^{bh}$ one has

$$E_x = \frac{\nu_b}{\omega_{cb}} E_y + \frac{2T}{e} \frac{1}{\sigma_p^b} \frac{\partial \sigma_p^b}{\partial x} \tag{A-4}$$

and

$$\frac{\partial \sigma_{po}}{\partial x} + \left[E_y \left(\frac{\nu}{\omega_c} - \frac{\nu_b}{\omega_{cb}}\right) \frac{e}{2T} - \frac{1}{\sigma_{po}^{b}} \frac{\partial \sigma_{po}^{b}}{\partial x}\right]\sigma_{po} = \sigma_{po}^{h} \frac{\nu}{\omega_c} E_y \frac{e}{2T} .$$

Fur purposes of estimates take $\frac{1}{\sigma_{po}^{b}} \frac{\partial \sigma_{po}^{b}}{\partial x} = \frac{1}{L_\perp(x)}$, and assume $\nu_b/\omega_{cb} \approx 3 \times 10^{-2}$, $T = 10^{3}$ °K and $E_y = 10^{-2}$ V/m. For the E region where $\nu/\omega_c \sim 1$, even for $L_\perp$ as small as 10^2 m, $\frac{eE_y}{2T} \frac{\nu}{\omega_c} L_\perp \approx 6$.

Then

$$\frac{\sigma_{po}}{\sigma^h_{po}} \approx 1 + \frac{\omega_c}{\nu} \frac{2T}{L_\perp(x)\, E_y e} \;(\approx 1\;) \quad ,$$

and:

$$\frac{1}{\sigma_{po}} \frac{\partial\sigma_{po}}{\partial x} \approx - \frac{\omega_c}{\nu} \frac{2T}{L_\perp(x) E_y e} \left(\frac{1}{L_\perp} \;\; \frac{dL_\perp}{dx} \right) .$$

For $L_\perp(x)$ a minimum, where one expects mode growth to be localized, $dL_\perp/dx = 0$ and $\frac{1}{\sigma_{po}} \frac{\partial\sigma_{po}}{\partial x} \ll \frac{1}{L_\perp(x)}$.

For the F region on the other hand $\nu/\omega_c \leqslant \nu_b/\omega_{cb}$ and

$$\frac{1}{\sigma_{po}} \frac{\partial\sigma_{po}}{\partial x} = \frac{1}{\sigma^b_{po}} \frac{\partial\sigma^b_{po}}{\partial x} - E_y \left(\frac{\nu}{\omega_c} - \frac{\nu_b}{\omega_{cb}} \right) \frac{e}{2T}$$

$$+ \frac{\sigma^h_{po}}{\sigma_{po}} \frac{\nu}{\omega_c} \frac{E_y e}{2T} \approx \frac{1}{\sigma^b_{po}} \frac{\partial\sigma^b_{po}}{\partial x} \quad .$$

Thus there are indications of possible contributions to growth from the zero-order F region; however, as noted, the time to set up a steady state in the F region would appear to be much greater than that for the E region and makes these estimates somewhat more tenuous for the F region. For the E region on the other hand, the indication is that inhomogeneities should be relatively unimportant.

Appendix B - Numerical Method

Here, we briefly outline the numerical procedure called BODEL (Dr. E. Graham, private communication) which was used to solve Eq. (22). First, Eq. (22) was written as four equations, each first order in the spatial derivative, by introducing the variables

$$V = \frac{\partial K}{\partial z} \tag{B-1}$$

so that we also have from Eq. (17)

$$\frac{\partial V}{\partial z} = \frac{\Gamma}{q_{\parallel o}} K + \frac{V}{\Gamma} \frac{\partial \Gamma}{\partial z} \tag{B-2}$$

where (B-1) and (B-2) are really four equations since V and K have real and imaginary parts (as does Γ). The real and imaginary part of the eigenvalue γ_1 were taken to satisfy the two equations

$$\frac{\partial \gamma_1}{\partial z} = 0 \tag{B-3}$$

We then have a sixth order system with six equations, six unknowns and six boundary conditions (Eqs. (23a),(23b) and (23c)). The finite difference equations are then obtained by making the substitutions

$$\frac{\partial f}{\partial z} \rightarrow (f_{i+1} - f_i)/\Delta z, \quad f \rightarrow \tfrac{1}{2}(f_{i+1} + f_i)$$

at the i th gridpoint (where f represents one of the six variables).

The system of finite-difference equations was solved by the Newton-Raphson iteration method. The ith of I equations ($I = 6$), at the kth gridpoint, is written as $F_i(u_{j,k}) = 0$, where there are I variables u_j, and M meshpoints. Let our nth approximation to the solution be the I by M matrix $u^n_{j,k}$. Then for $u^{n+1}_{j,k} = u^n_{j,k} + \delta u_{j,k}$, substitution in the system and linearizing gives

$$F_i(u_{j,k}) + \sum_{j,k}\left(\partial F_i/\partial u_{j,k}\right)\delta u_{j,k} = 0$$

which is a system of I equations at each meshpoint. This I by M system is solved by Gaussian elimination using pivotal condensation with back substitution. The matrix is block bi-diagonal, since at the k-1/2 th point, the functions depend only on the values at the k and k-1 st meshpoints. The Jacobian matrix itself, $\partial F/\partial u$, is found through numerical differencing. The subprogram which perform these operations are all part of the BODEL language. We iterate until the maximum residual (value of F_i) is below an error criterion, taken throughout this work as 10^{-8}. The boundary conditions are treated similarly. No differencing need be done on the boundaries.

Appendix C - The diffusion coefficient for barium ions in a homogeneous ionosphere with stationary electrons

We consider a barium layer with small inhomogeneity in the x direction and an ionospheric layer at a different altitude but with the same generalized potential, $\psi(x,y)$. For the barium ions we have

$$- \underline{v}_b \times \underline{\omega}_{cb} + \nu_b \underline{v}_b = - \frac{T_b}{n_b m_b} \nabla n_b + e \frac{\underline{E}_b}{m_b} \tag{C-1}$$

where $\underline{E}_b$ is the electric field at the barium level and $\underline{\omega}_{cb} = \omega_{cb} \underline{B}/|B|$. For the ionospheric ions, we have

$$- \underline{v}_i \times \underline{\omega}_{ci} + \nu_i \underline{v}_i = \frac{e\underline{E}_i}{m_i} \tag{C-2}$$

where $\underline{E}_i$ is the electric field at the ionospheric level. Since $(\nabla_\perp \psi)_b = (\nabla\psi)_i$ we have on assuming equal ion and electron temperatures

$$\underline{E} \equiv \underline{E}_{\perp b} = \underline{E}_{\perp i} - \frac{T_b}{e} \frac{\nabla n_b}{n_b} \tag{C-3}$$

from which on integrating over the barium and ionospheric layers separately we obtain

$$\int n_i \underline{v}_i dz = \frac{\Sigma_p^i \underline{E}}{e} \tag{C-4}$$

and

$$\int n_b \underline{v}_b dz = \frac{\Sigma_p^b \underline{E}}{e} - \frac{2T}{e^2} \nabla \Sigma_p^b \tag{C-5}$$

Since the electrons are stationary

$$\int n_i \underline{v}_i dz = - \int n_b \underline{v}_b dz$$

and

$$\int n_b \underline{v}_b dz = - \frac{2T}{e^2} \frac{\Sigma_p^i}{\Sigma_p^i + \Sigma_p^b} \nabla \Sigma_p^b$$

From the continuity equation we have

$$\frac{\partial}{\partial t} \int n_b dz + \nabla \cdot \int n_b \underline{v}_b dz = 0$$

Since the spatial inhomogeneity is small, this results in:

$$\frac{\partial}{\partial t} \int n_b dz - \frac{2T}{e} \frac{\Sigma_p^i}{\Sigma_p^i + \Sigma_p^b} \frac{\frac{\nu_c}{\omega_{cb}}}{1 + \left(\frac{\nu_c}{\omega_{cb}}\right)^2} \frac{c}{B} \nabla^2 \int n_b dz = 0$$

and this has the form

$$\frac{\partial}{\partial t} \int n_b dz = D_{eff} \nabla^2 \int n_b dz$$

with an effective diffusion coefficient, D_{eff},

$$D_{eff} = \frac{2T}{eB} \frac{\Sigma_p^i}{\Sigma_p^b + \Sigma_p^i} \frac{\nu_b/\omega_{cb}}{1 + (\nu_b/\omega_{cb})^2} \tag{C-6}$$

The result of Eq. (31) follows from using $\Sigma_p{}^i = \Sigma_{pr}{}^i(k) + i\Sigma_{pi}{}^i(k)$ and taking the real part of D_{eff}.

Appendix D - Partial coupling to the F region

From Eq. (13) on assuming no current as $z \to \infty$, one obtains

$$\psi_1(z) - \psi_1(\infty) = \int_\infty^z \frac{1}{\sigma_{\|o}} dz' \int_\infty^{z'} \Gamma \, \psi_1(z'') dz'' \qquad \text{(D-1)}$$

On writing

$$\Gamma = \Gamma_o + \Gamma_1$$

where

$$\Gamma_o = k^2 \sigma_{po}$$

and

$$\Gamma_1 = k^2 \sigma_{po} \frac{ikL_\perp \, \nu/\omega_c \Big/ \left(1 + \frac{\nu^2}{\omega_c^2}\right)}{\gamma_1 - \frac{ikL_\perp \, \nu/\omega_c}{1 + \frac{\nu^2}{\omega_c^2}}}$$

we may expand

$$\psi_1 = \psi_{10} + \psi_{11} + \ldots \qquad \text{(D-2)}$$

to obtain

$$\psi_{10}(z) - \psi_{10}(\infty) = \int_{\infty}^{z} \frac{1}{\sigma_{\|o}} dz' \int_{\infty}^{z'} \Gamma_o \psi_{10}(z'')dz'' \qquad \text{(D-3a)}$$

$$\psi_{11}(z) - \psi_{11}(\infty) = \int_{\infty}^{z} \frac{1}{\sigma_{\|o}} dz' \int_{\infty}^{z'} \Gamma_o \psi_{11}(z'')dz''$$

$$+ \int_{\infty}^{z} \frac{1}{\sigma_{\|o}} dz' \int_{\infty}^{z'} \Gamma_1 \psi_{10}(z'')dz'' \qquad \text{(D-3b)}$$

where

$$\psi_1(z_1) \equiv \psi_{10}(z_1) = 1 \quad ,$$

$$\psi_{11}(z_1) = 0$$

and z_1 denotes the altitude of the "top" of the barium cloud.

If, as is expected for partial coupling to the F region, one has $\psi_{10}(\infty) \neq 0$, then $\psi_{10}(z)$ monotonically decreases in magnitude as z increases. We may use this to show from (D-3a) that:

$$\psi_{10}(\infty) \leq 1/[1 + \alpha(z_1)] \quad , \qquad \text{(D-4)}$$

where:

$$\alpha(z) = \int_{\infty}^{z} \frac{1}{\sigma_{\|o}} dz' \int_{\infty}^{z'} \Gamma_o dz'' \quad . \qquad \text{(D-4a)}$$

By similar algebra, for any $z^* \ni z_1 < z^* < \infty$ we may show

$$\psi_{10}(\infty) \geq \left(1 - \int_{z^*}^{z_1} \frac{1}{\sigma_{\|o}} dz' \int_{z^*}^{z_1} \Gamma_o dz''\right) / \Delta \tag{D-5}$$

where

$$\Delta = \left\{1 + [\alpha(z^*) + \int_{z^*}^{z_1} \frac{1}{\sigma_{\|o}} dz' \int_{\infty}^{z^*} \Gamma_o dz'']\right\}[1 + \alpha(z^*)].$$

The right hand side (D-5) becomes the right hand side of (D-4) for:

$$I \equiv \int_{z^*}^{z_1} \frac{1}{\sigma_{\|o}} dz' \int_{z^*}^{z_1} \Gamma_o dz'' \ll 1 \tag{D-6}$$

and

$$\alpha(z^*) \ll 1 \quad . \tag{D-7}$$

On the other hand for the transition from partial to total coupling one seeks by virtue of (D-4) that:

$$\alpha(z_1) \sim 1 \; . \tag{D-8}$$

We identify z^* with the bottom of the F region conductivity maximum and assume negligible potential drop between z^* and ∞. [This is equivalent to condition (D-7).] For $z^* = 280$ km and our solarmax conditions the left hand sides of (D-6), (D-7) and (D-8) are respectively:

$0.04/\lambda^2$, $0.05/\lambda^2$ and $1/\lambda^2$, λ in km. For $z^* = 270$ km and our solarmin conditions the left hand sides of (D-6), (D-7) and (D-8) are respectively $5 \times 10^{-3}/\lambda^2$, $6 \times 10^{-3}/\lambda^2$ and $3.2 \times 10^{-2}/\lambda^2$. Hence on neglect of terms of relative size $\approx .2$,

$$\psi_{10}(\infty) = 1/[1 + \alpha(z_1)] \qquad \text{(D-9a)}$$

for $\lambda \geq 0.5$ km and solarmax conditions or $\lambda \geq 0.2$ km and solarmin conditions. Since (D-9a) results from replacing $\psi_{10}(z'')$ by $\psi_{10}(\infty)$ within (D-3a) one expects to within similar accuracy:

$$\psi_{10}(z) = \frac{1 + \alpha(z)}{1 + \alpha(z_1)} \quad , \; z_1 < z < \infty \; . \qquad \text{(D-9b)}$$

We next demonstrate that in these wavelength ranges the contributions from $\psi_{11}(z)$ are small. The imaginary part of Γ_1 is bounded in magnitude by $\Gamma_o\delta$, with $\delta = - kL_\perp \nu_i/\omega_{ci}\gamma_{1r}$, while the real part of Γ_1 is bounded by $\Gamma_o\delta/2$. To simplify the analysis we consider Γ_1 to be approximated by its imaginary part.

On replacing $\psi_{11}(z'')$ by $\psi_{11}(\infty)$ in (D-3b) and defining

$$\beta(z) \equiv \int_\infty^z \frac{1}{\sigma_{\|o}} dz' \int_\infty^{z'} \Gamma_1\psi_{10}(z'')dz'' \qquad \text{(D-10)}$$

we obtain

$$\psi_{11}(\infty) = - \frac{\beta(z_1)}{1 + \alpha(z_1)} \qquad \text{(D-11)}$$

which itself can be used to obtain

$$\psi_{11}(z) = -\beta(z_1)\frac{[1+\alpha(z)]}{[1+\alpha(z_1)]} + \beta(z) \qquad \text{(D-12)}$$

This procedure is self-consistent if $\psi_{11}(z) \approx$ constant for $z > z^*$ and:

$$\left|\int_{z^*}^{\infty} \Gamma_o \psi_{11}(\infty) dz'\right| > \left|\int_{z_1}^{z^*} \Gamma_o \psi_{11}(z') dz'\right| \qquad \text{(D-13)}$$

From (D-11) and (D-12) we have:

$$[\psi_{11}(z) - \psi_{11}(\infty)]/\psi_{11}(\infty) = \alpha(z) - \beta(z)/\beta(z_1) - \beta(z)\alpha(z_1)/\beta(z_1). \qquad \text{(D-14a)}$$

Since $\Gamma_1\psi_{10}(z)/i\Gamma_o$ is monotonically decreasing with increasing z, by successive applications of the mean value theorem, it can be shown that $\beta(z)/\beta(z_1) < \alpha(z)/\alpha(z_1)$. Hence on using the estimates for (D-6) - (D-8) for $z > z^*$:

$$\left|[\psi_{11}(z) - \psi_{11}(\infty)]/\psi_{11}(\infty)\right| < 0.2.$$

Further, from, (D-11) and (D-12) one has:

$$\frac{\psi_{11}(\infty)}{\psi_{11}(z)} \geq \frac{1}{1+\alpha(z_1)} \quad . \qquad \text{(D-14b)}$$

For solarmax conditions we take $\alpha(z_1) \leq 4$ and $\int_{z^*}^{\infty} \Gamma_o dz' / \int_{z}^{z^*} \Gamma_o dz' \approx 30$;

for solarmin conditions we take $\alpha(z_1) \leq 1$ and $\int_{z^*}^{\infty} \Gamma_o dz' / \int_{z}^{z^*} \Gamma_o dz' \approx 6$;

hence (D-13) is satisfied.

To show that our basic expansion (D-3a) and (D-3b) is valid we observe from (D-12) and (D-9b):

$$r(z) \equiv \frac{-i}{[1+\alpha(z_1)]} \frac{\psi_{11}(z)}{\psi_{10}(z)} = \frac{-i\beta(z)}{1+\alpha(z)} + \frac{i\beta(z_1)}{1+\alpha(z_1)} . \tag{D-15}$$

Further we have $r(z_1) = 0$, $r(\infty) = \dfrac{i\beta(z_1)}{1+\alpha(z_1)} < 0$, and

$$r'(z) = \frac{(-i\beta') + \alpha(-i\beta)(\beta'/\beta - \alpha'/\alpha)}{(1+\alpha)^2}$$

with $-i\beta > 0$ and $-i\beta' < 0$. Since $\nu_i \psi_{10}/\omega_{ci}$ is a monotonically decreasing function for increasing z, by using the mean value theorem on β'/β one can show

$$\beta'/\beta - \alpha'/\alpha < 0 \quad .$$

Hence, $r'(z) < 0$ and $|r(\infty)| > |r(z)|$, $z < \infty$, or equivalently:

$$|\psi_{11}(z)/\psi_{10}(z)| < |\psi_{11}(\infty)/\psi_{10}(\infty)|$$

for $z < \infty$. Thus the expansion (D-2) is valid to the extent that $|r(\infty)| = | - \beta(z_1)| \ll 1$.

But we note on decomposing $-\beta(z_1)$ into component double integrals:

$$r(\infty) = -\int_{\infty}^{z^*} \frac{1}{\sigma_{\|o}} dz' \int_{\infty}^{z'} \Gamma_1 dz'' - \int_{z^*}^{z_1} \frac{1}{\sigma_{\|o}} dz' \int_{\infty} \Gamma_1 dz''$$

$$-\int_{z^*}^{z_1} \frac{1}{\sigma_{\|o}} dz' \int_{z^*}^{z'} \Gamma_1 \, dz'' \quad . \tag{D-16}$$

The first term is approximated by

$$- i \; \frac{\alpha(z^*) kL_\perp}{\gamma_{1r}} \; \frac{< \nu_i/\omega_{ci} >}{1 + \alpha(z_1)} \tag{D-17}$$

where $< \nu_i/\omega_{ci} >$ represents an average over the region $z > z^*$.

The second term is approximated by

$$- i \; \frac{\alpha(z_1)}{1 + \alpha(z_1)} \; \frac{kL_\perp < \nu_i/\omega_{ci} >}{\gamma_{1r}} \; . \tag{D-18}$$

The third term is approximated by

$$- i \; I \; kL_\perp \; [\nu_i/\omega_{ci}(200)]/\gamma_{1r} \quad , \tag{D-19}$$

where I is defined in (D-6) and $[\nu_i/\omega_{ci}(200)]$ denotes the value of ν_i/ω_{ci} at $z = 200$ km.

Expressions (D-17) - (D-19) are peaked at large k. Under solar-maximum conditions with $\lambda \geq 0.5$ km, we have $< \nu_i/\omega_{ci} > < 10^{-2}$, $kL_\perp \leq 12.6$, $\alpha\ (z^*) \leq 0.2$, $\alpha\ (z_1) \leq 4$, $[\nu_i/\omega_{ci}(200)] = 0.03$, $I \leq 0.16$ and $\gamma_{1r} \approx -0.9$. Then (D-17), (D-18) and (D-19) are respectively

bounded by 0.01 i, 0.12 i, and 0.07 i, and $|r(\infty)| < 0.22$. Under solarminimum conditions with $\lambda \geq 0.2$ km, we have $< \nu_i/\omega_{ci} > \leq 2 \times 10^{-3}$, $kL_\perp \leq 31.4$, $\alpha(z^*) \leq 0.15$, $\alpha(z_1) \leq 0.81$, $[\nu_i/\omega_{ci}(200)] = 0.014$ and $I \leq 0.125$. For $\Sigma_p{}^b/\Sigma_p{}^i = 4.0$ (and $\gamma_{1r} \approx -0.9$), (D-17), (D-18) and (D-19) are respectively bounded by 0.01i, 0.04i and 0.06i and $|r(\infty)| < 0.12$. For $\Sigma_p{}^b/\Sigma_p{}^i = 0.2$ (and $\gamma_{1r} \approx -1/3$) we have $|r(\infty)| < 0.33$.

Hence $|r(\infty)| < 1$ in all cases and the expansion (D-2) with $\psi_{10}(z)$ given by (D-9b) appears valid over the asserted wavelength ranges.

Appendix E - Coupling from counter-streaming ion diffusion for short wavelengths

For sufficiently short wavelengths the background ionosphere is effectively homogeneous. Here we provide an estimate of the effect of coupling for a barium cloud such that $\sigma^{i}_{po}/\sigma^{b}_{po} \ll 1$ where σ^{i}_{po} and σ^{b}_{po} are the local ionospheric Pedersen conductivity and barium Pedersen conductivity. A somewhat similar estimate for small barium clouds has been carried out by Perkins et al. [1973]. However, imaging effects involving $kL_{\perp}\nu/\omega_c$ were neglected and the assumption was made that the region of ionospheric homogeneity was sufficiently large that its integrated Pedersen conductivity could be comparable with the integrated barium Pedersen conductivity.

The first order potential is described by Eq. (13):

$$\Gamma\psi_1 = \frac{d}{dz}\left(\sigma_{\|o} \frac{d\psi_1}{dz}\right) \tag{E-1}$$

Above and below the barium cloud ($z > z_1$ and $z < z_o$, respectively) one has: $\Gamma = \Gamma_i = \dfrac{k^2\sigma^{i}_{po}\gamma_1}{\gamma_1 - ikL_{\perp}\nu/\omega_c}$, $\sigma_{\|o} = \sigma^{i}_{\|o}$. For the region of the barium cloud ($z_1 > z > z_o$) one has:

$$\Gamma = \Gamma_t = \Gamma_i + k^2\sigma^{b}_{po}(\gamma_1 + 1)/(\gamma_1 - ikL_{\perp}\nu_b/\omega_{cb})$$

$$\sigma_{\|o} = \sigma^{i}_{\|o}\ (1 + \frac{n_b}{n_i})$$

where n_b and n_i are the barium number density and the ionospheric number density respectively. Within each of the three regions by assumption of homogeneity one has

$$\Gamma\psi_1 = \sigma_{\|o} \frac{\partial^2\psi_1}{\partial z^2} .$$

Across z_1 and z_o one has that ψ_1 and $\sigma_{\|o} \; \partial\psi_1/\partial z$ are continuous. Further one has the requirements $\psi_1(z = z_1 + L_\|)/\psi_1(z_1) \ll 1$ and $\psi_1(z = z_o - L_\|)/\psi_1(z_o) \ll 1$ where $L_\|$ is an ionospheric scale length; this leads to the variation

$$\psi_1 \sim e^{-(\Gamma_i/\sigma^i_{\|o})^{1/2}(z-z_1)} , \; z > z_1 \tag{E-2}$$

$$\psi_1 \sim e^{(\Gamma_i/\sigma^i_{\|o})^{1/2}(z-z_o)} , \; z < z_o \tag{E-3}$$

with $\mathrm{Re}(\Gamma_i/\sigma^i_{\|o})^{1/2} > 0$.

From (E-1) we obtain

$$\int_{z_o-L_\|}^{z_1+L_\|} \Gamma\psi_1 dz = 0$$

On anticipating that $\psi_1(z) \approx$ constant for $z_o < z < z_1$ (as may be verified self-consistently for $\gamma_1 \approx -1$ and $\sigma^b_p \gg \sigma^i_p$)for a wide range of k such that $\mathrm{Re}(\Gamma_1/\sigma^i_{\|o})^{-1/2} < L_\|$ we obtain, with $L_{\|b} = z_1 - z_o$,

$$\Gamma_t L_{\|b} + \Gamma_i/(\Gamma_i/\sigma^i_{\|o})^{1/2}\Big|_{z=z_1} + \Gamma_i/(\Gamma_i/\sigma^i_{\|o})^{1/2}\Big|_{z=z_o} = 0 \tag{E-4}$$

It is clear for order of magnitude estimates that we can evaluate each of the ionospheric contributions at the barium level.

On assuming $\sigma^i_{po}/\sigma^b_{po} \ll 1$ (and consequently $\gamma_1 \approx -1$), Eq. (E-4) results in:

$$\gamma_1 = -1 + \frac{\sigma^i_{po}}{\sigma^b_{po}} \frac{[1 + (kL_\perp)^2(\nu/\omega_c)(\nu_b/\omega_{cb})]}{1 + (kL_\perp \nu/\omega_c)^2}$$

$$+ \frac{\sqrt{2}}{kL_{\|b}} \frac{(\sigma^i_{po}\, \sigma^i_{\|o})^{1/2}}{\sigma^b_{po}} \left(\frac{\left\{[1 + (kL_\perp \nu/\omega_c)^2]^{1/2} + 1\right\}^{1/2}}{\sqrt{1 + (kL_\perp \nu/\omega_c)^2}} \right.$$

$$\left. + kL_\perp(\nu_b/\omega_{cb}) \left\{[1 + (kL_\perp \nu/\omega_c)^2]^{1/2} - 1\right\}^{1/2} \right)$$

$$+ i \left[\frac{\sigma^i_{po}}{\sigma^b_{po}} kL_\perp \frac{(\nu_b/\omega_{cb} - \nu/\omega_c)}{[1 + (kL_\perp \nu/\omega_c)^2]} \right.$$

$$+ \frac{\sqrt{2}}{kL_{\|b}} \frac{(\sigma^i_{po}\sigma^i_{\|o})^{1/2}}{\sigma^b_{po}} \frac{1}{[1 + (kL_\perp \nu/\omega_c)^2]^{1/2}}$$

$$\Big((kL_\perp \nu_b/\omega_{cb}) \left\{[1 + (kL_\perp \nu/\omega_c)^2]^{1/2} + 1\right\}^{1/2}$$

$$\left. - \left\{[1 + (kL_\perp \nu/\omega_c)^2]^{1/2} - 1\right\}^{1/2} \Big) \right] .$$

We note: $\gamma/(c\mathcal{E}/BL_\perp) = \gamma_1 \left(-1 + 2i \dfrac{kT}{e\mathcal{E}}\right)$. For short wavelengths one has $2Tk/e\mathcal{E} \gg 1$ and

$$\gamma_r \approx \frac{c\mathcal{E}}{BL_\perp}\left\{1 - \frac{2T}{e\mathcal{E}}\, k\, \frac{\sigma^i_{po}}{\sigma^b_{po}}\left[\frac{kL_\perp(\nu_b/\omega_{cb} - \nu/\omega_c)}{[1 + (kL_\perp\nu/\omega_c)^2]}\right.\right.$$

$$+ \frac{\sqrt{2}}{kL_{\|b}}\left(\frac{\sigma^i_{\|o}}{\sigma^i_{po}}\right)^{1/2} \frac{1}{[1 + (kL_\perp\nu/\omega_c)^2]^{1/2}}$$

$$\left((kL_\perp\nu_b/\omega_{cb})\left\{[1 + (kL_\perp\nu/\omega_c)^2]^{1/2} + 1\right\}^{1/2}\right.$$

$$\left.\left.\left. - \left\{[1 + (kL_\perp\nu/\omega_c)^2]^{1/2} - 1\right\}^{1/2}\right)\right]\right\} .$$

As k increases for either $kL_\perp\nu/\omega_c \ll 1$ or $kL_\perp\nu/\omega_c \gg 1$, γ_r decreases. Hence the maximum value of γ_r for short wavelengths occurs for k such that the solution is just localized. This is estimated by $\mathrm{Re}(\sigma^i_{\|o}/\Gamma_i)^{1/2} = L_\|$ with $\gamma_1 = -1$ and yields

$$k = \sqrt{2\eta^2+1}\;\omega_{ci}/L_\perp\nu_i\eta^2$$

with $\eta = \sqrt{2}\,\dfrac{L_\|}{L_\perp}\left(\dfrac{\nu_e/\omega_{ce}}{\nu_i/\omega_{ci}}\right)^{1/2}$. Characteristically one has $\nu_e/\omega_{ce} = 10^{-3}\,\nu_i/\omega_{ci}$, $L_\|/L_\perp = 20, \eta = 1$, and $\nu_b/\omega_{cb} = \sqrt{7}\,\nu_i/\omega_{ci}$.

This results in

$$\gamma_r = \frac{c\mathcal{E}}{BL_\perp}\left(1 - 9.4\,\frac{T}{e\mathcal{E}} - k\,\frac{\sigma^{\,i}_{po}}{\sigma^{\,b}_{po}}\right) .$$

References

Farley, D. T., Jr., "A Theory of Electrostatic Fields in a Horizontally Stratified Ionosphere Subject to a Vertical Magnetic Field," J. Geophys. Res., 64, 1225, 1959.

Farley, D. T., Jr., "A Theory of Electrostatic Fields in the Ionosphere at Nonpolar Geomagnetic Latitudes," J. Geophys. Res., 65, 869, 1960.

Goldman, S. R., "Barium Cloud Striation Structure," Bull. Am. Phys. Soc., 11, 1269, 1971.

Goldman, S. R., S. L. Ossakow, and D. L. Book, "On the Nonlinear Motion of a Small Barium Cloud in the Ionosphere," J. Geophys. Res., 79, 1471, 1974.

Hanson, W. B., "Structure of the Ionosphere," in Satellite Environment Handbook, edited by F. S. Johnson, Stanford Univ. Press, Stanford, Calif. 1961.

Johnson, F. S., "Structure of the Upper Atmosphere," in Satellite Environment Handbook, edited by F. S. Johnson, Stanford University Press, Stanford, Calif., 1961.

Kindel, J. M., and C. F. Kennel, "Topside Current Instabilities," J. Geophys. Res., 76, 3055, 1971.

Linson, L. M., and J. B. Workman," Formation of Striations Ionospheric Plasma Clouds," J. Geophys. Res., 75, 3211, 1970.

Lloyd, K. H., and G. Haerendel, "Numerical Modeling of the Drift and Deformation of Ionospheric Plasma Clouds and of Their

Interaction with Other Layers of the Ionosphere," J. Geophys. Res., 78, 7389, 1973.

Perkins, F. W., N. J. Zabusky, and J. H. Doles III, "Deformation and Striation of Plasma Clouds in the Ionosphere, 1, " J. Geophys. Res., 78, 697, 1973.

Perkins, F. W., and J. H. Doles III, "Velocity Shear and the E X B Instability," J. Geophys. Res., 80, 211, 1975.

Scannapieco, A. J., S. L. Ossakow, D. L. Book, B. E. McDonald, and S. R. Goldman, "Conductivity Ratio Effects on the Drift and Deformation of F Region Barium Clouds Coupled to the E Region Ionosphere," J. Geophys. Res., 79, 2913, 1974.

Shiau, J. H., and A. Simon, "Onset of Striations in Barium Clouds," Phys. Rev. Lett., 29, 1664, 1972.

Simon, A., "Growth and Stability of Artificial Ion Clouds in the Ionosphere," J. Geophys. Res., 75, 6287, 1970.

Simon, A., and A. M. Sleeper, "Barium Cloud Growth in a Highly Conducting Medium," J. Geophys. Res., 77, 2353, 1972.

Spreiter, J. R., and B. R. Briggs, "Theory of Electrostatic Fields in the Ionosphere at Polar and Middle Geomagnetic Latitudes," J. Geophys. Res., 66, 1731, 1961.

Swift, D. W., "Effective Height-Integrated Conductivity of the Ionosphere," J. Geophys. Res., 77, 1279, 1972.

Völk, H. J., and G. Haerendel, "Striations in Ionospheric Ion Clouds, 1," J. Geophys. Res., 76, 4541, 1971.

Zabusky, N. J., J. H. Doles, III, and F. W. Perkins, "Deformation and Striation of Plasma Clouds in the Ionosphere, 2, Numerical Simulation of a Nonlinear Two-Dimensional Model," J. Geophys. Res., 78, 711, 1973.

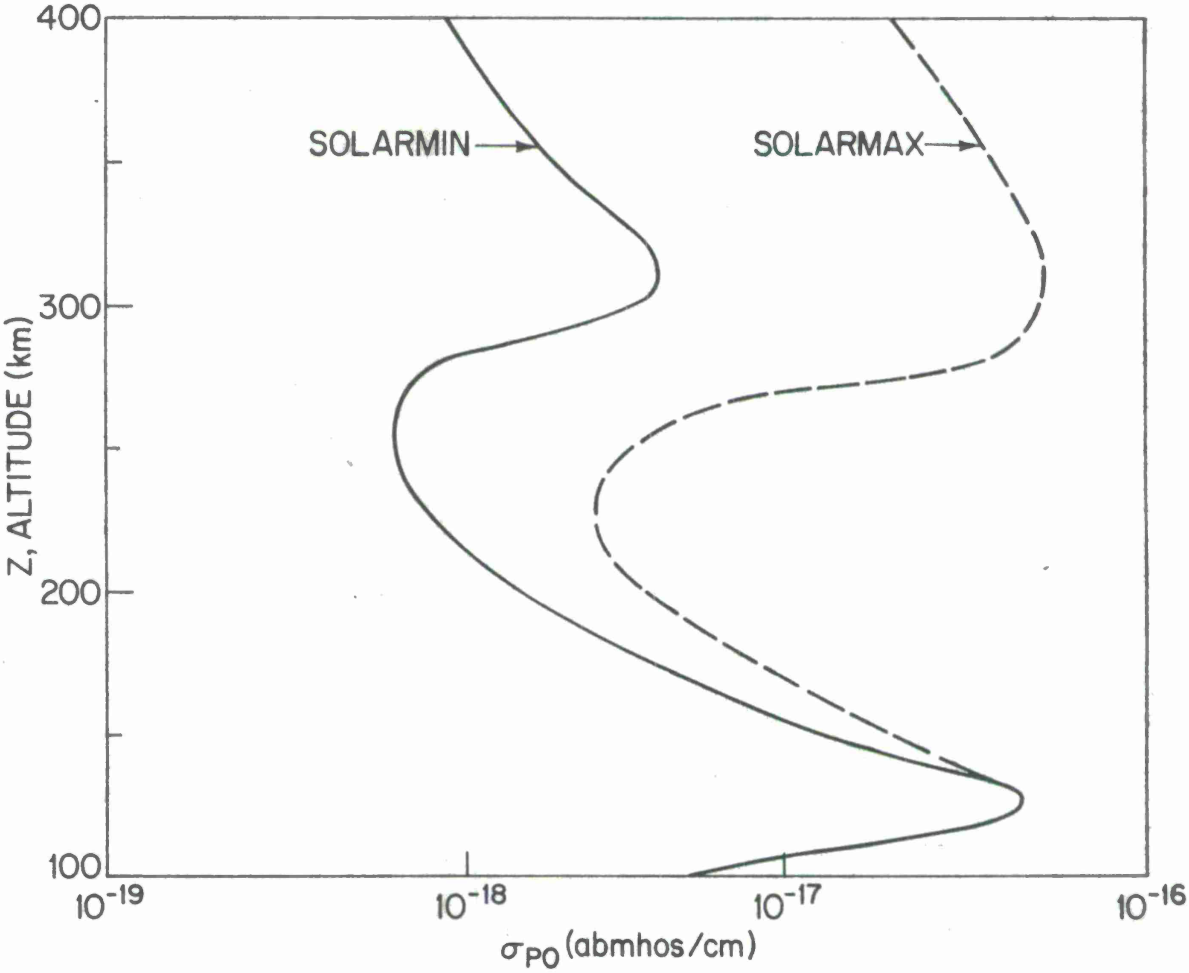

Fig. 1 — Zero order Pedersen conductivity, σ_{po}, vs altitude at nighttime solarmax and solarmin conditions. These are basically the values given by *Hanson* [1961], correcting the error in his curve for solarmin below the E region peak. The curves are consistently based on *Hanson's* [1961] curves for the ambient electron density and ion-neutral collision frequency vs altitude using B = 0.4 gauss and an ionic mass equal to the neutral atmospheric mass as given by *Johnson* [1961]. To obtain the units of mhos/m multiply the values given in this figure by 10^{11}.

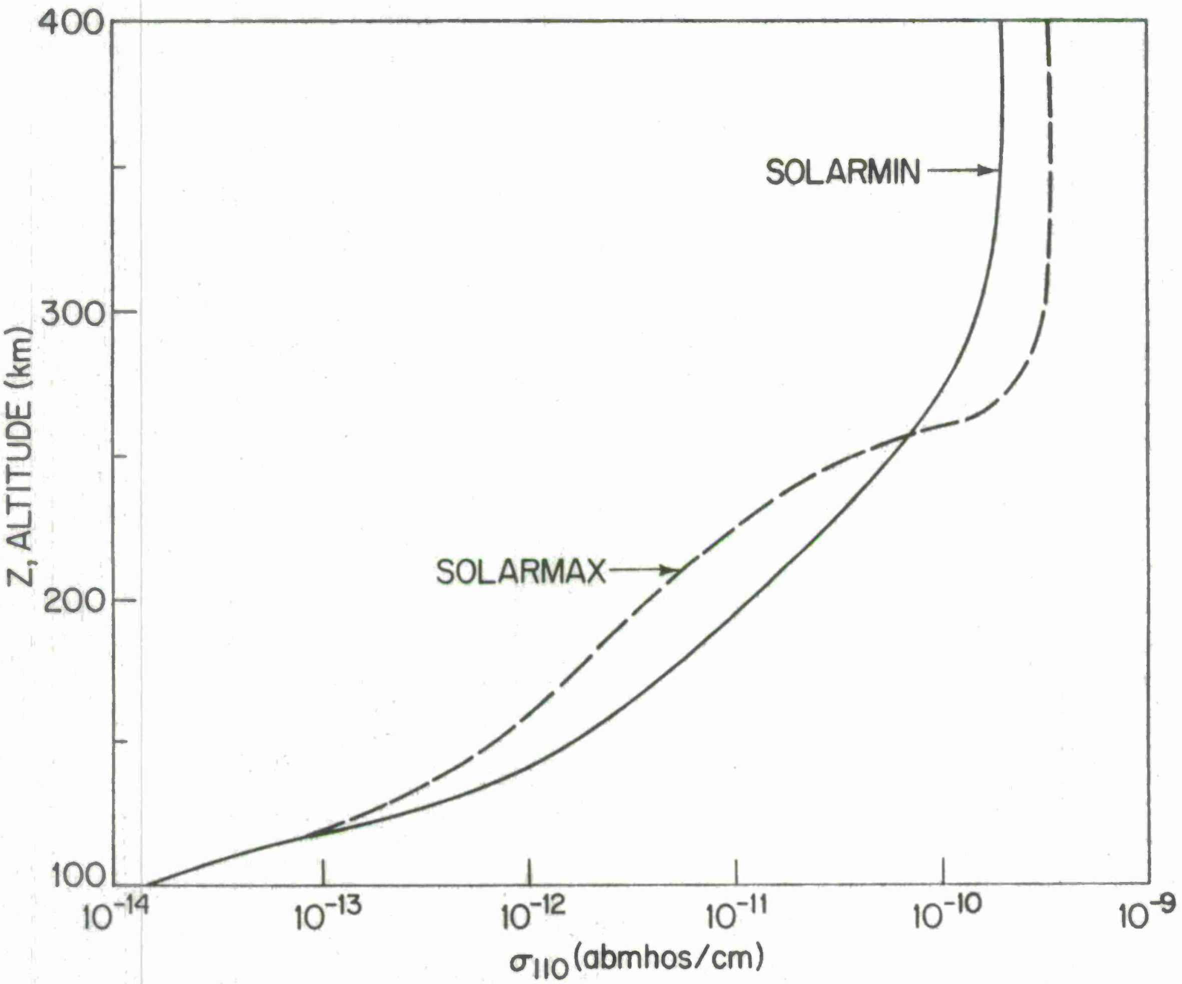

Fig. 2 — Zero order parallel conductivity, $\sigma_{\|0}$, vs altitude, at nighttime solarmax and solarmin conditions. To obtain the units of mhos/m multiply the values given in this figure by 10^{11}.

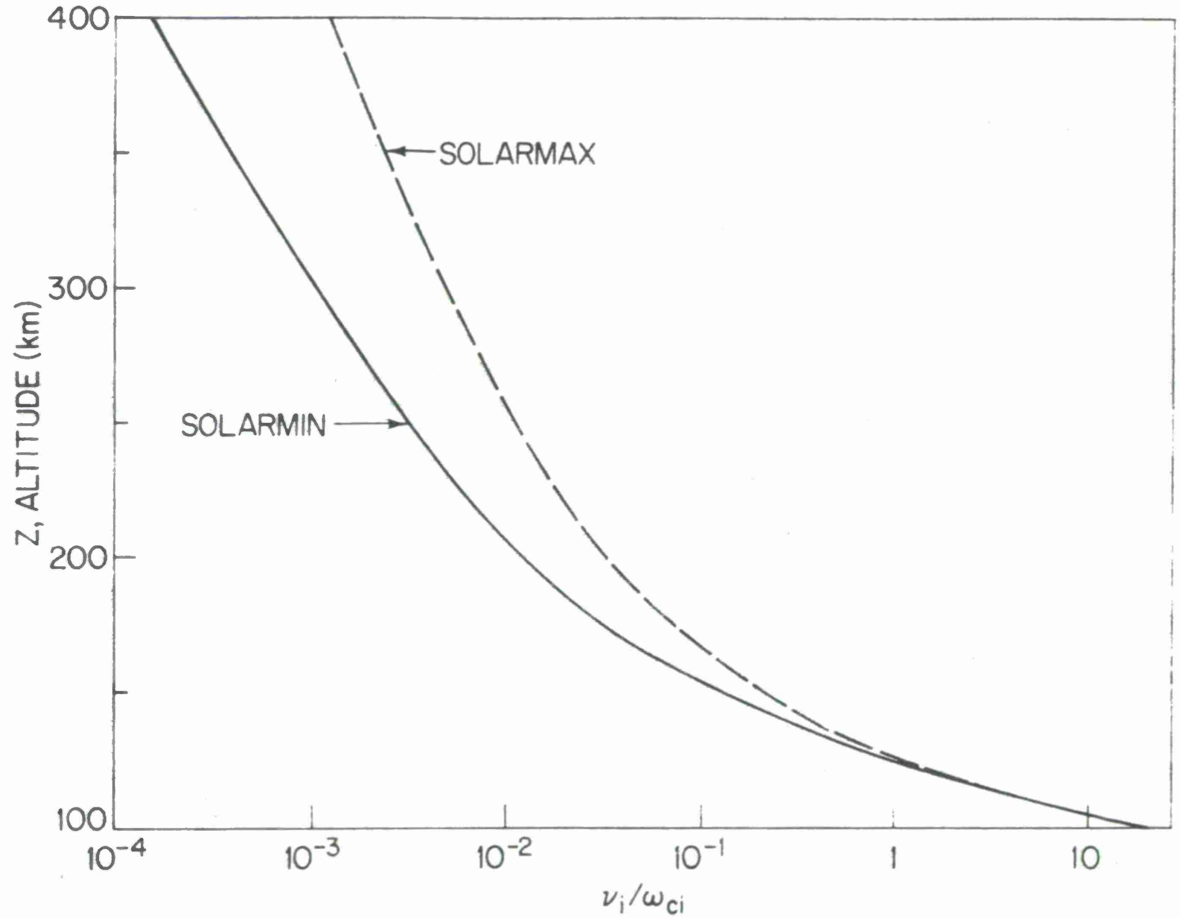

Fig. 3 — Ratio of ion-neutral collision frequency to ion cyclotron frequency, ν_i/ω_{ci}, vs altitude for solarmax and solarmin conditions. The values of ν_i are taken from *Hanson* [1961] and ω_{ci} is computed using B = 0.4 gauss and an ionic mass equal to the neutral atmospheric mass as given by *Johnson* [1961].

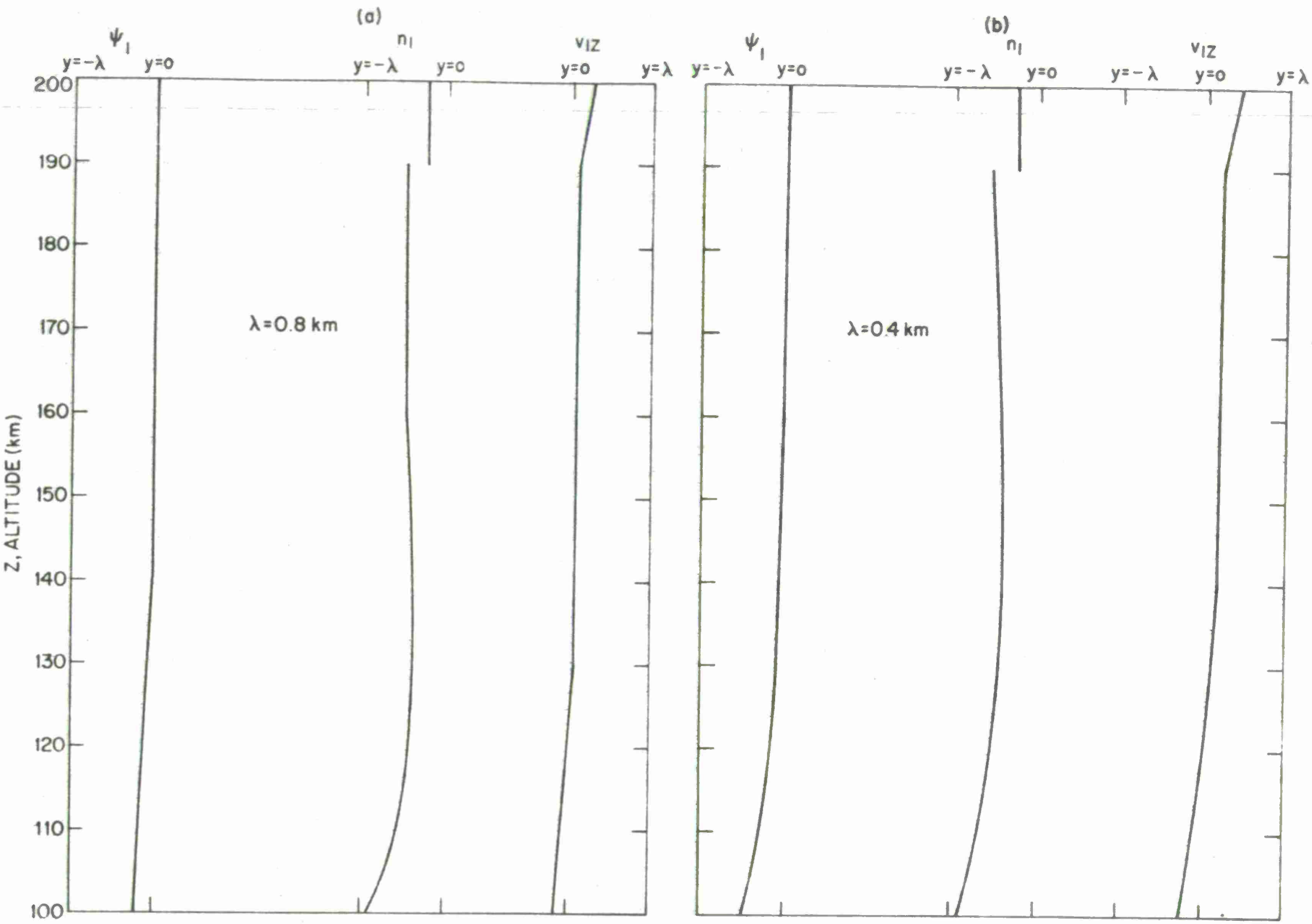

Fig. 4 — Phase variation in modal structure-zero phase locations drawn as a function of altitude, z, given that ψ_1 at z = 190 km and y = 0 is at zero phase. Contours are reflected around y = 0 for $B_z < 0$. a) Case I, λ = 0.8 km, b) Case II, λ = 0.4 km, where we have taken $\mathcal{E}$ = 5mV/m and T = 10^3 ^{0}K.

CASE I

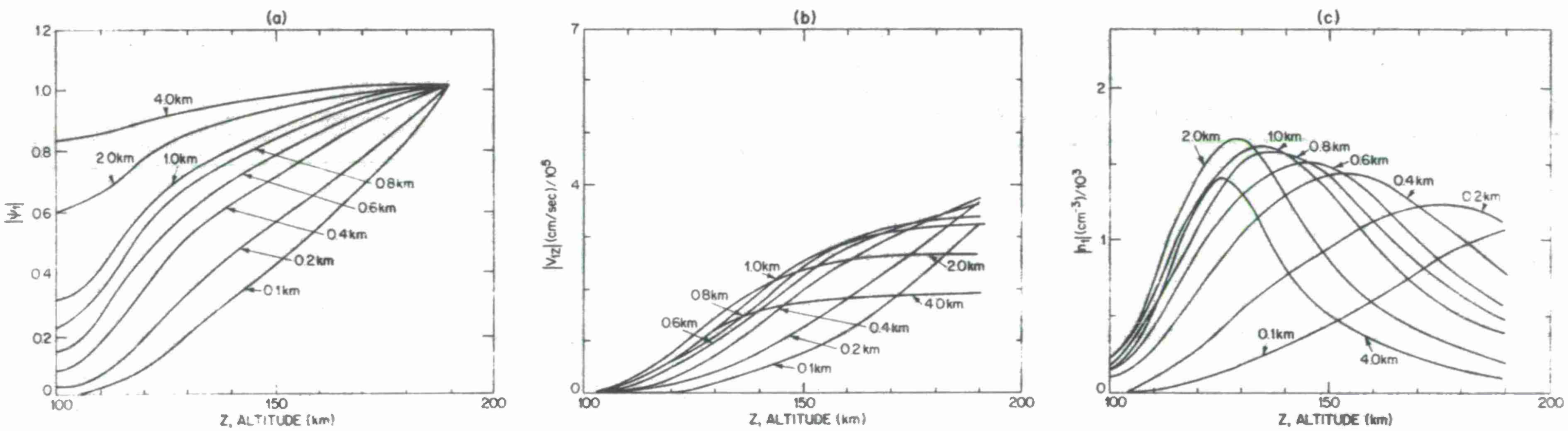

Fig. 5 — Case I, a) $|\psi_1(z)|$ as a function of altitude and wavelength, λ (perpendicular to the magnetic field in the y direction and equal to $2\pi/k$) normalized to $|\psi_1(190)| = 1$, b) $|v_{1z}(z)|$ as a function of altitude and wavelength, λ, with $\psi_1(190) = \mathcal{E}/k$, c) $|n_1(z)|$ as a function of altitude and wavelength, λ, with $\psi_1(190) = \mathcal{E}/k$. For b) and c), if $\psi_1 = \alpha\mathcal{E}/k$ then n_1 and v_{1z} in the figure should be multiplied by α.

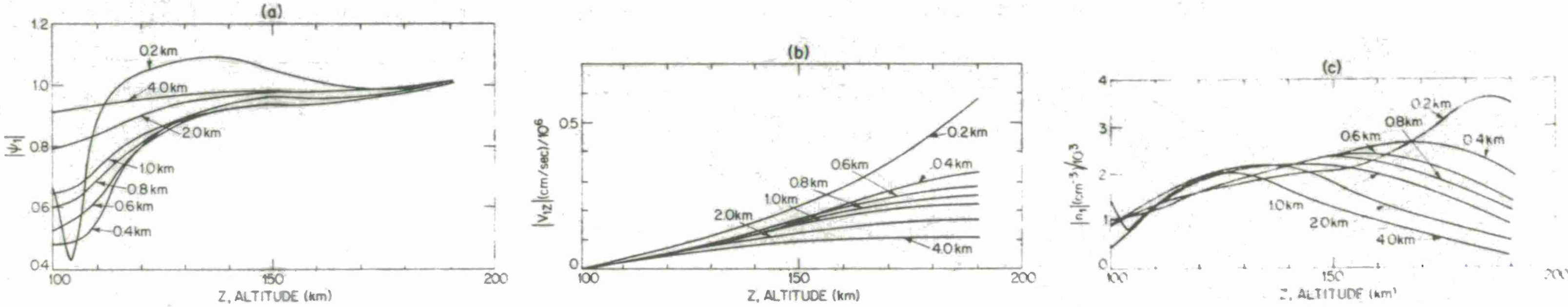

Fig. 6 — Case II, a) $|\psi_1(z)|$ as a function of altitude and wavelength, λ (perpendicular to the magnetic field in the y direction and equal to $2\pi/k$) normalized to $|\psi_1(190)| = 1$, b) $|v_{1z}(z)|$ as a function of altitude and wavelength, λ, with $\psi_1(190) = \mathcal{E}/k$, c) $|n_1(z)|$ as a function of altitude and wavelength, λ, with $\psi_1(190) = \mathcal{E}/k$. For b) and c), if $\psi_1 = \alpha\mathcal{E}/k$ then n_1 and v_{1z} in the figure should be multiplied by α.

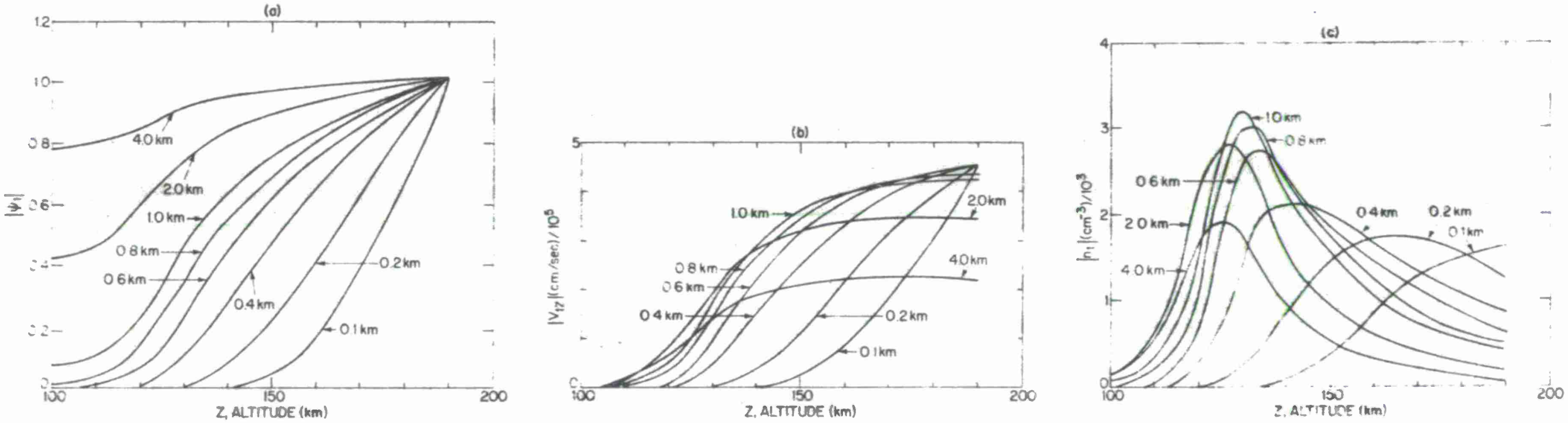

Fig. 7 — Case III, a) $|\psi_1(z)|$ as a function of altitude and wavelength, λ (perpendicular to the magnetic field in the y direction and equal to $2\pi/k$) normalized to $|\psi_1(190)| = 1$, b) $|v_{1z}(z)|$ as a function of altitude and wavelength, λ, with $\psi_1(190) = \mathcal{E}/k$, c) $|n_1(z)|$ as a function of altitude and wavelength, λ, with $\psi_1(190) = \mathcal{E}/k$. For b) and c), if $\psi_1 = \alpha\mathcal{E}/k$ then n_1 and v_{1z} in the figure should be multiplied by α.

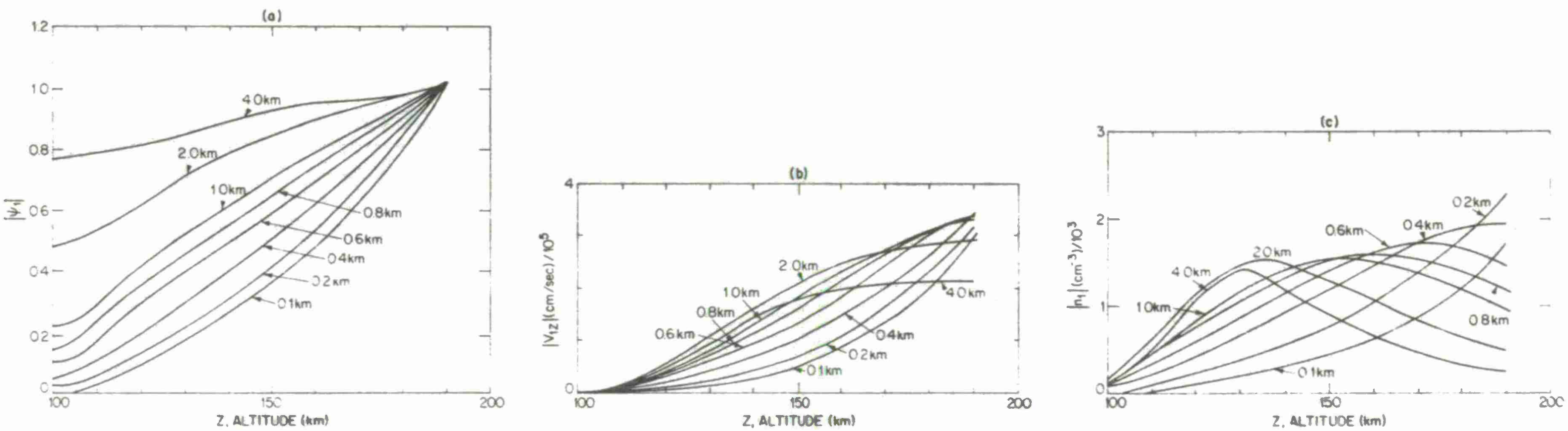

Fig. 8 — Case IV, a) $|\psi_1(z)|$ as a function of altitude and wavelength, λ (perpendicular to the magnetic field in the y direction and equal to $2\pi/k$) normalized to $|\psi_1(190)| = 1$,b) $|v_{1z}(z)|$ as a function of altitude and wavelength, λ, with $\psi_1(190) = \mathcal{E}/k$, c) $|n_1(z)|$ as a function of altitude and wavelength, λ, with $\psi_1(190) = \mathcal{E}/k$. For b) and c), if $\psi_1 = \alpha\mathcal{E}/k$ then n_1 and v_{1z} in the figure should be multiplied by α.

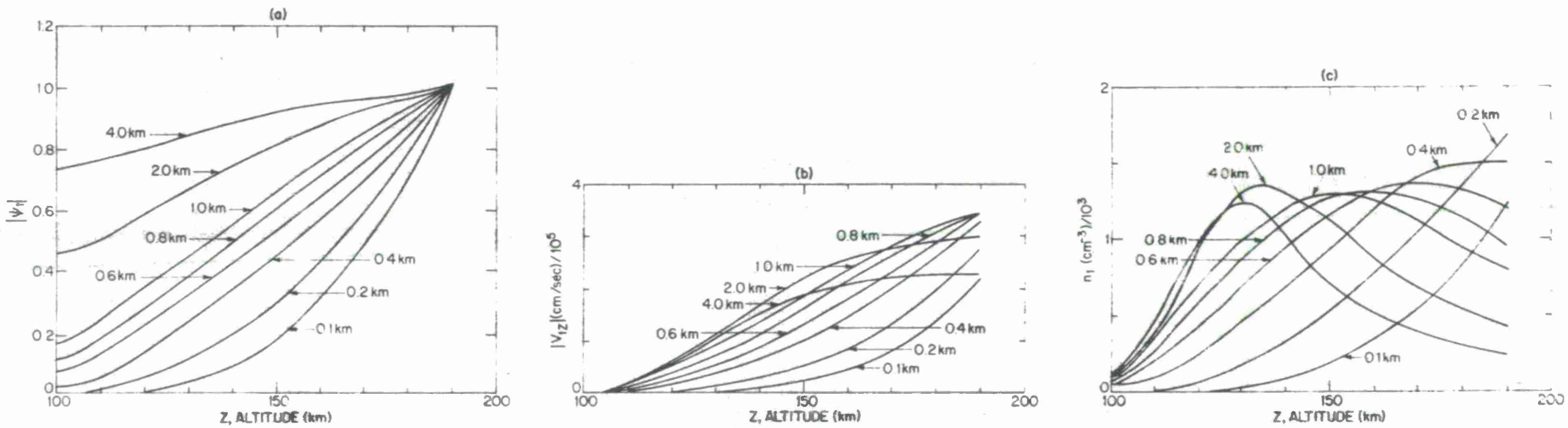

Fig. 9 — Case V, a) $|\psi_1(z)|$ as a function of altitude and wavelength, λ (perpendicular to the magnetic field in the y direction and equal to $2\pi/k$) normalized to $|\psi_1(190)| = 1$, b) $|v_{1z}(z)|$ as a function of altitude and wavelength, λ, with $\psi_1(190) = \mathcal{E}/k$, c) $|n_1(z)|$ as a function of altitude and wavelength, λ, with $\psi_1(190) = \mathcal{E}/k$. For b) and c), if $\psi_1 = \alpha\mathcal{E}/k$ then n_1 and v_{1z} in the figure should be multiplied by α.

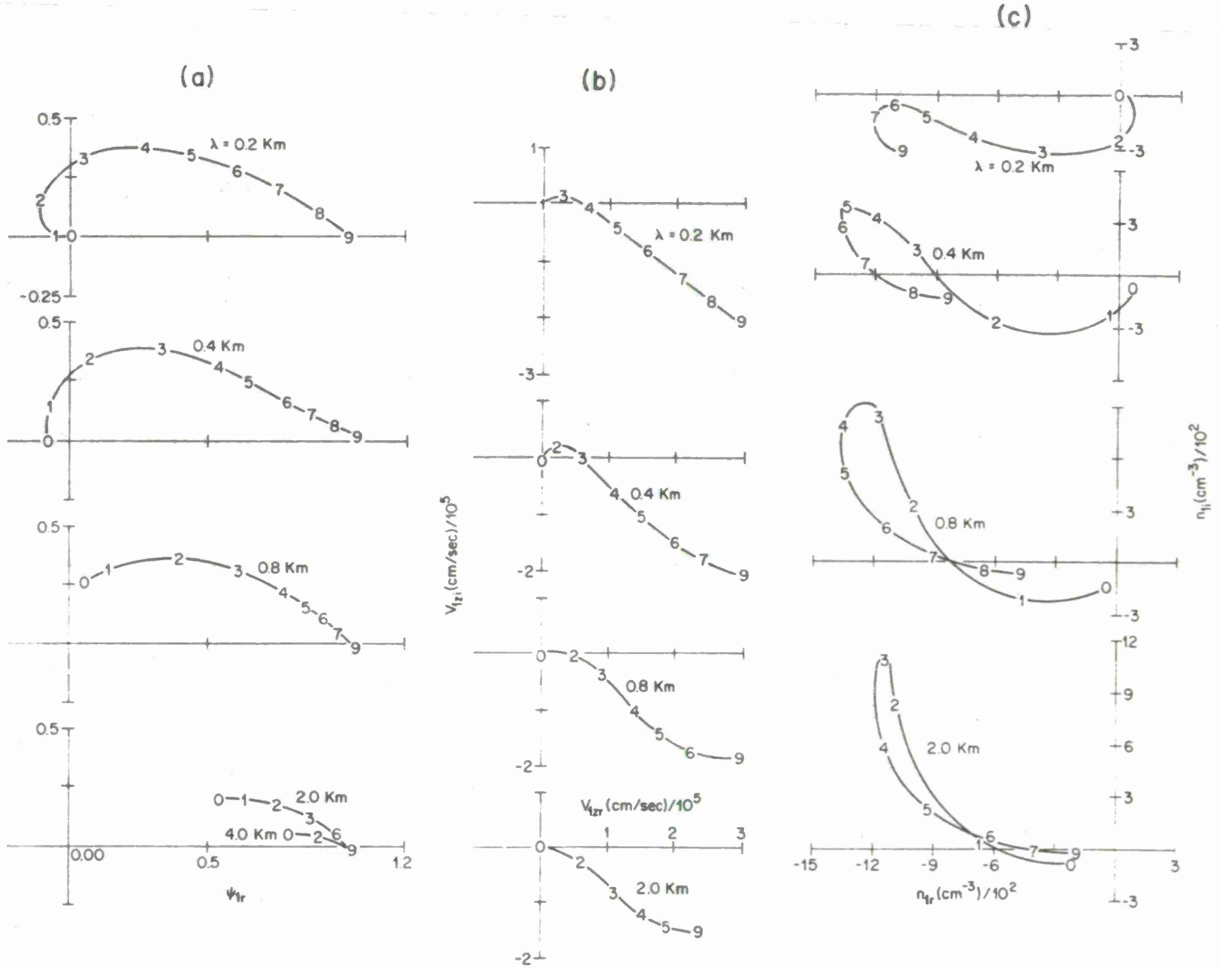

Fig. 10 — Hodographs for Case I. Digits m along curves indicate values at altitudes given by (100 + 10m) km. a) $\psi_{1i}(z)$ vs $\psi_{1r}(z)$. $|\psi 1(z)|$ is given by distance from origin. The striation structure has period λ along y. Locations in phase with $\psi_1(190)$ at y = 0 are given by $y = -\xi(z)\lambda/2\pi$ where $\xi(z)$ is the polar angle. b) $v_{1zi}(z)$ vs $v_{1zr}(z)$. $|v_{1z}(z)|$ is given by distance from origin. Locations in phase with $\psi_1(190)$ are given by $y = -\xi(z)$ $\lambda/2\pi$ where $\xi(z)$ is the polar angle. c) $n_{1i}(z)$ vs $n_{1r}(z)$. $|n_1(z)|$ is given by distance from origin. Locations in phase with $\psi_1(190)$ are given by $y = -\xi(z)\lambda/2\pi$, where $\xi(z)$ is the polar angle.

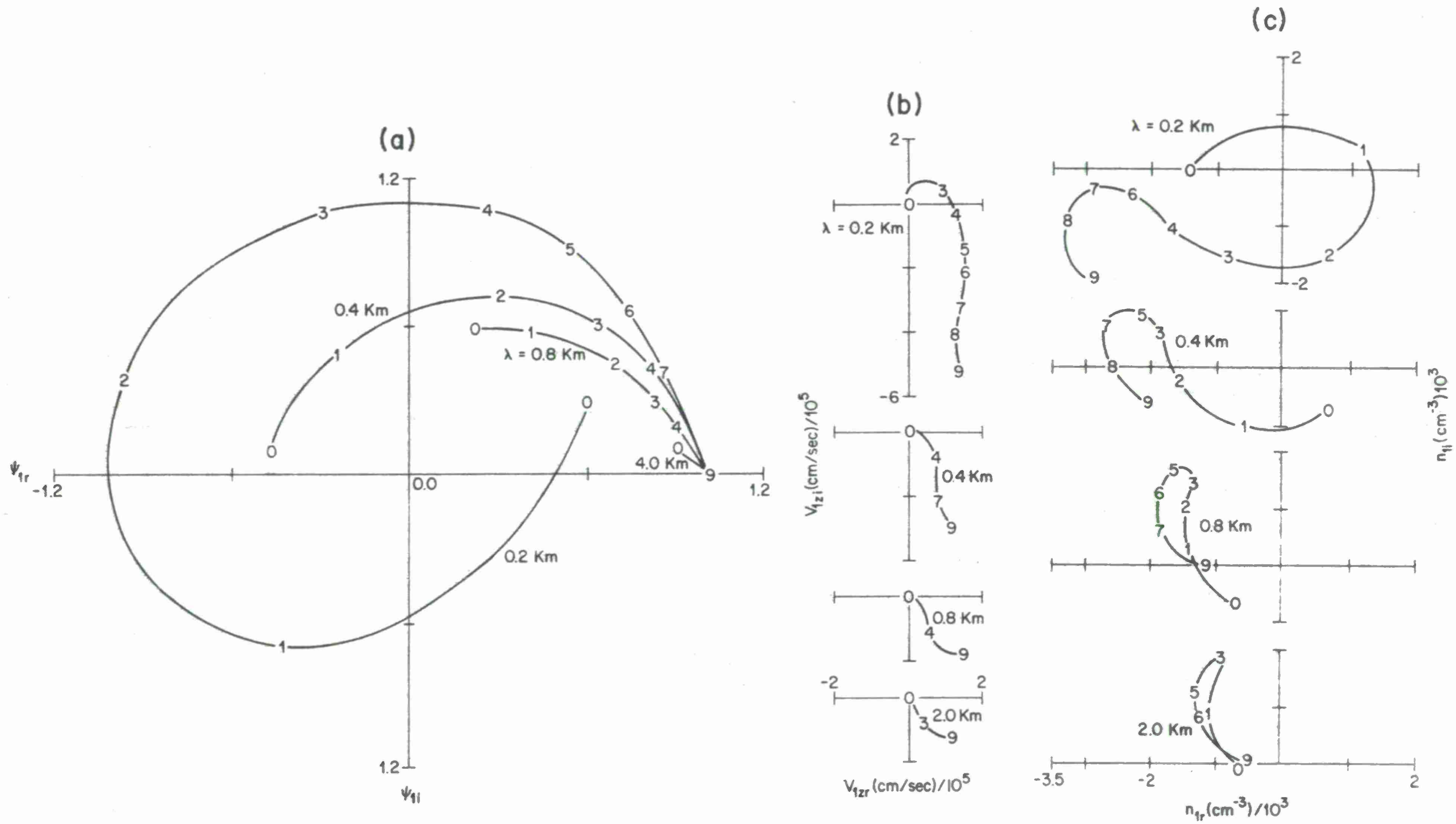

Fig. 11 — Hodographs for Case II. Digits m along curves indicate values at altitudes given by (100 + 10m) km. a) $\psi_{1i}(z)$ vs $\psi_{1r}(z)$. $|\psi_1(z)|$ is given by distance from origin. The striation structure has period λ along y. Locations in phase with $\psi_1(190)$ at $y = 0$ are given by $y = -\xi(z)\lambda/2\pi$ where $\xi(z)$ is the polar angle. b) $v_{1zi}(z)$ vs $v_{1zr}(z)$. $|v_{1z}(z)|$ is given by distance from origin. Locations in phase with $\psi_1(190)$ are given by $y = -\xi(z)\lambda/2\pi$ where $\xi(z)$ is the polar angle. c) $n_{1i}(z)$ vs $n_{1r}(z)$. $|n_1(z)|$ is given by distance from origin. Locations in phase with $\psi_1(190)$ are given by $y = -\xi(z)\lambda/2\pi$, where $\xi(z)$ is the polar angle.

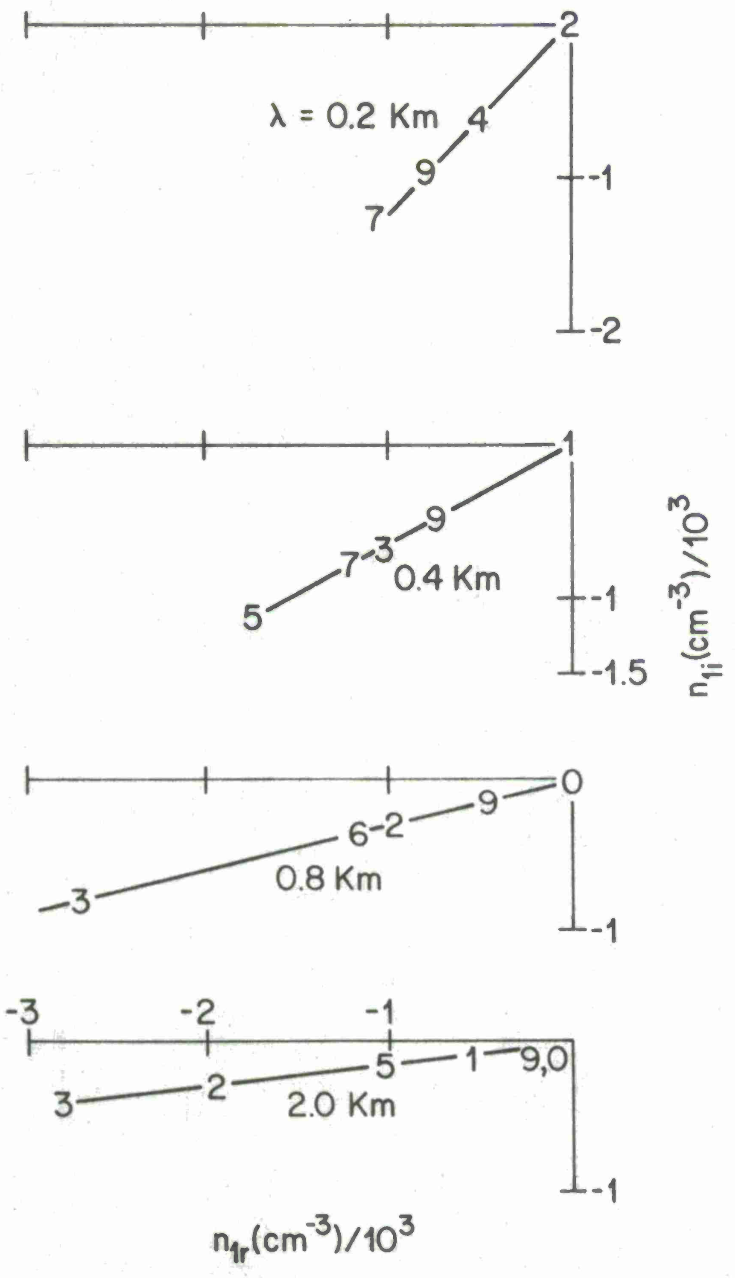

Fig. 12 — Hodographs for Case III. Digits m along curves indicate values at altitudes given by (100 + 10m) km. $n_{1i}(z)$ vs $n_{1r}(z)$. $|n_1(z)|$ is given by distance from origin. Locations in phase with $\psi_1(190)$ are given by $y = -\xi(z)\lambda/2\pi$, where $\xi(z)$ is the polar angle, but note $d\xi/dz = 0$.

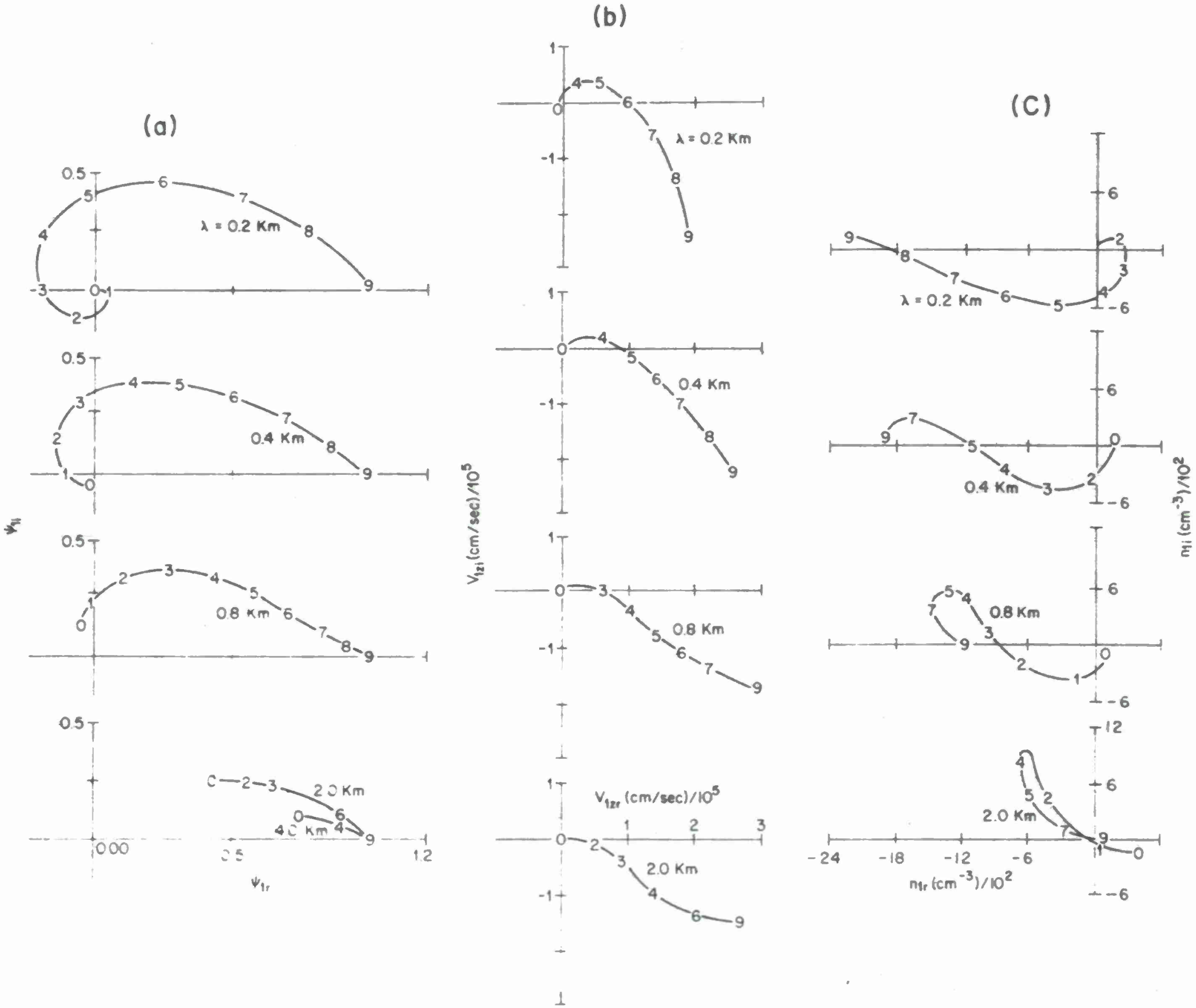

Fig. 13 — Hodographs for Case IV. Digits m along curves indicate values at altitude given by (100 + 10m) km. a) $\psi_{1i}(z)$ vs $\psi_{1r}(z)$. $|\psi_1(z)|$ is given by distance from origin. The striation structure has period λ along y. Locations in phase with $\psi_1(190)$ at y = 0 are given by $y = -\xi(z)\lambda/2\pi$ where $\xi(z)$ is the polar angle. b) $v_{1zi}(z)$ vs $v_{1zr}(z)$. $|v_{1z}(z)|$ is given by distance from origin. Locations in phase with $\psi_1(190)$ are given by $y = -\xi(z)\lambda/2\pi$ where $\xi(z)$ is the polar angle. c) $n_{1i}(z)$ vs $n_{1r}(z)$. $|n_1(z)|$ is given by distance from origin. Locations in phase with $\psi_1(190)$ are given by $y = -\xi(z)\lambda/2\pi$, where $\xi(z)$ is the polar angle.

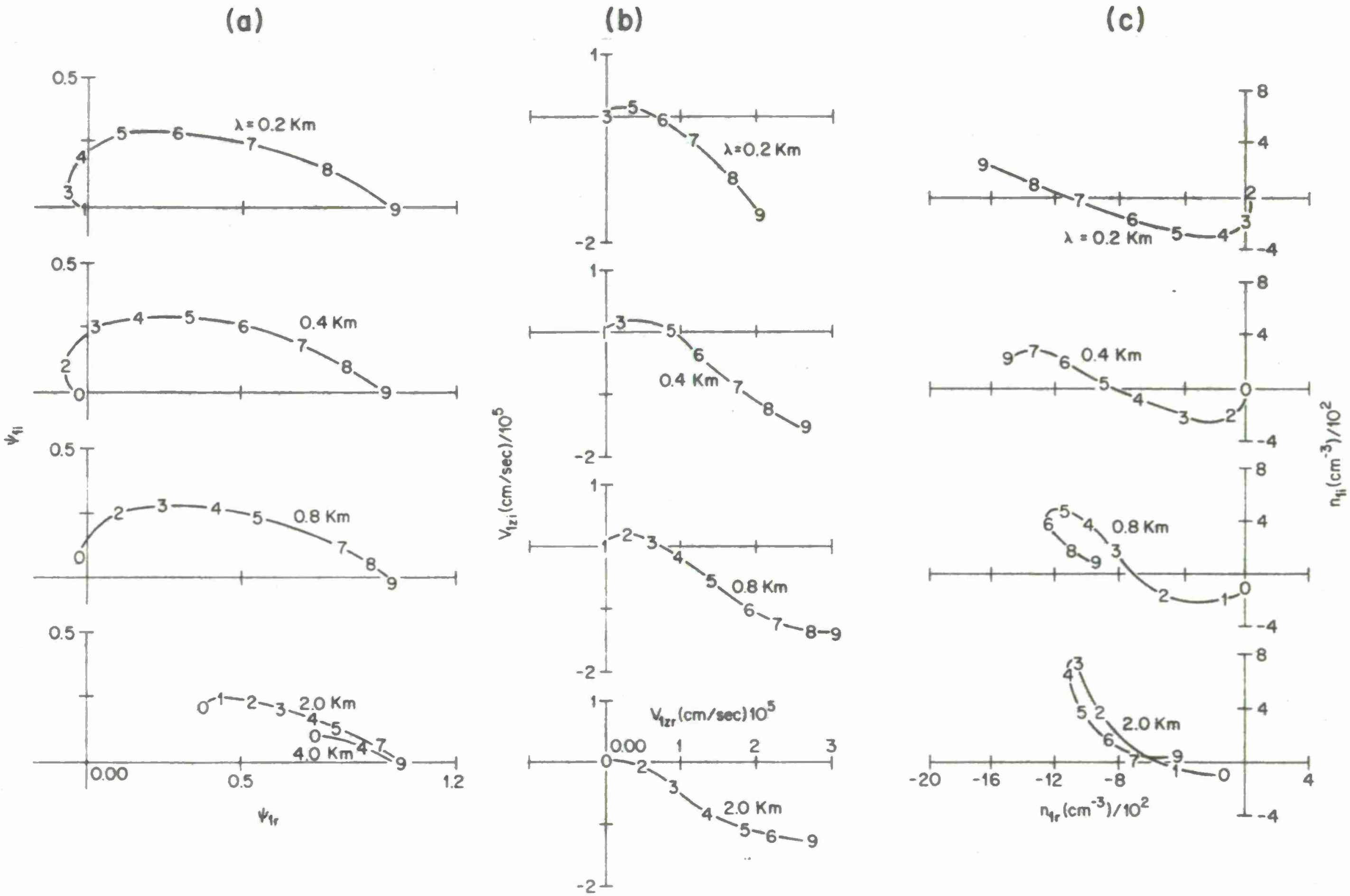

Fig. 14 — Hodographs for Case V. Digits m along curves indicate values at altitudes given by (100 + 10m) km. a) $\psi_{1i}(z)$ vs $\psi_{1r}(z)$. $|\psi_1(z)|$ is given by distance from origin. The striation structure has period λ along y. Locations in phase with $\psi_1(190)$ at y = 0 are given by $y = -\xi(z)\lambda/2\pi$ where $\xi(z)$ is the polar angle. b) $v_{1zi}(z)$ vs $v_{1zr}(z)$. $|v_{1z}(z)|$ is given by distance from origin. Locations in phase with $\psi_1(190)$ are given by $y = -\xi(z)\lambda/2\pi$ where $\xi(z)$ is the polar angle. c) $n_{1i}(z)$ vs $n_{1r}(z)$. $|n_1(z)|$ is given by distance from origin. Locations in phase with $\psi_1(190)$ are given by $y = -\xi(z)\lambda/2\pi$, where $\xi(z)$ is the polar angle.

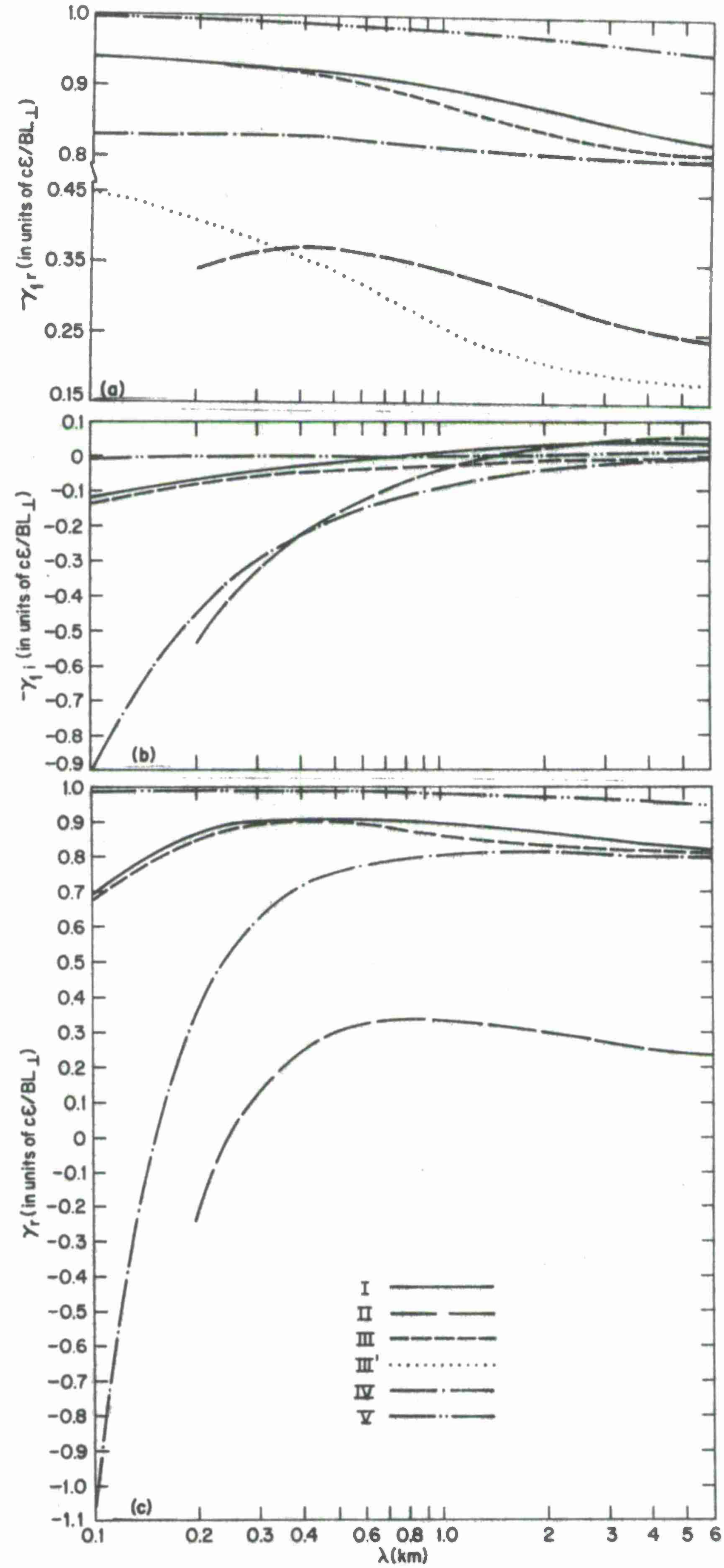

Fig. 15 — Eigenvalues for Cases (I) - (V). a) the zero temperature growth rate, $-\gamma_{1r}$, in units of $c\mathcal{E}/BL_\perp$. "III'" refers to $\Sigma_p^b/\Sigma_p^i = 0.2$, but with neglect of image density transport; b) $-\gamma_{1i}$, the zero temperature frequency in units of $c\mathcal{E}/BL_\perp$; c) γ_r, the growth rate appropriate to $T = 10^3$ °K, $\mathcal{E}$ = 5mV/m, in units of $c\mathcal{E}/BL_\perp$. [Eq. (15) with $d\gamma_1/dz = 0$, relates γ to γ_1.]

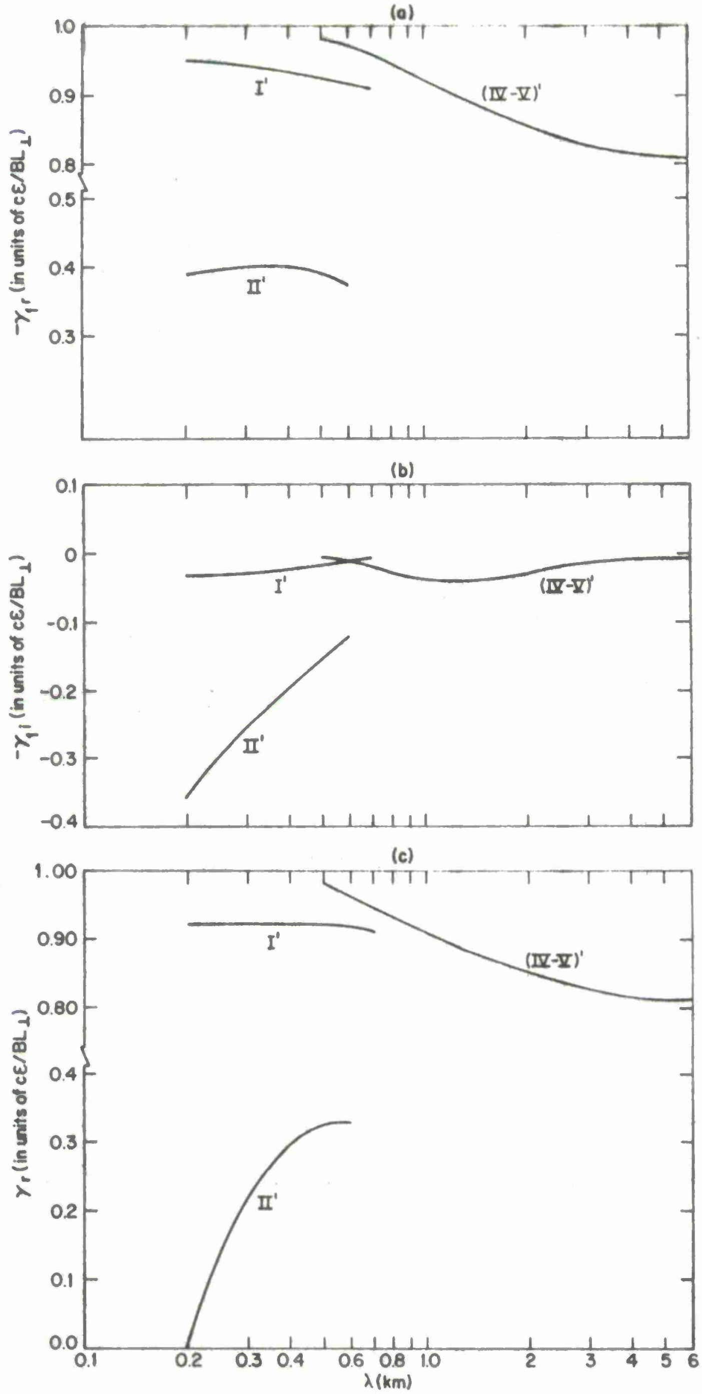

Fig. 16 — Eigenvalues with partial coupling. I′ denotes Σ_p^b/Σ_p^i = 4.0, solarmin conditions with partial coupling; II′ denotes Σ_p^b/Σ_p^i = 0.2, solarmin conditions with partial coupling; (IV-V)′ denotes Σ_p^b/Σ_p^i = 4.0, solarmax conditions with partial coupling. I (Fig. 15) and I′ are the same for $\lambda \geqslant 0.7$ km. II (Fig. 15) and II′ are the same for $\lambda \geqslant 0.6$ km. (IV-V)′ goes smoothly into V (Fig. 15) for $\lambda \leqslant 0.5$ km. a) $-\gamma_{1r}$, b) $-\gamma_{1i}$, c) γ_r. [Eq. (15) with $d\gamma_1/dz = 0$, relates to γ to γ_1.]

DISTRIBUTION LIST

DIRECTOR
Defense Advanced Rsch Proj Agency
Architect Building
1400 Wilson Blvd.
Arlington, VA 22209
ATTN: Strategic Tech Office

Defense Communication Engineer Center
1860 Wiehle Avenue
Reston, VA 22090
ATTN: CODE R820 R. L. Crawford

Defense Communication Engineer Center
1960 Wiehle Avenue
Reston, VA 22090
ATTN: CODE R410 W. D. Dehart

DIRECTOR
Defense Communications Agency
Washington, D. C. 20305
ATTN: CODE 960

DIRECTOR
Defense Communications Agency
Washington, D. C. 20305
ATTN: CODE 480

Defense Documentation Center
Cameron Station
Alexandria, VA 22314 — 12 copies (if open publication)
ATTN: TC — 2 copies (if otherwise)

DIRECTOR
Defense Intelligence Agency
Washington, D. C. 20301
ATTN: W. Wittig DC-7D

DIRECTOR
Defense Intelligence Agency
Washington, D. C. 20301
ATTN: DT-1B

DIRECTOR
Defense Nuclear Agency
Washington, D. C. 20305
ATTN: STSI Archives

DIRECTOR
Defense Nuclear Agency
Washington, D. C. 20305
ATTN: STVL

DISTRIBUTION LIST
(Continued)

DIRECTOR
Defense Nuclear Agency
Washington, D. C. 20305 — 2 copies
ATTN: STTL Tech Library

DIRECTOR
Defense Nuclear Agency
Washington, D. C. 20305
ATTN: DDST

DIRECTOR
Defense Nuclear Agency
Washington, D. C. 20305
ATTN: RAAE

DIR OF DEFENSE RSCH & ENGINEERING
Washington, D. C. 20301
ATTN: DD/S&SS John B. Walsh

DIR OF DEFENSE RSCH & ENGINEERING
Washington, D. C. 20301
ATTN: OAD/EPS LTC W. A. Whitaker

COMMANDER
Field Command
Defense Nuclear Agency
Kirtland AFB, NM 87115
ATTN: FCPR

COMMANDER
Field Command
Defense Nuclear Agency
Kirtland AFB, NM 87115
ATTN: FCPR COL. John P. Hill

Interservice Nuclear Weapons School
Kirtland AFB, NM 87115
ATTN: Document Control

DIRECTOR
Joint Strat TGT Planning Staff Jcs
Offutt AFB
Omaha, NM 68113
ATTN: JLTW-2

DIRECTOR
Joint Strat TGT Planning Staff Jcs
Offutt AFB
Omaha, NB 68113
ATTN: JPST G. D. Burton

DISTRIBUTION LIST
(Continued)

DIRECTOR
Joint Strat TGT Planning Staff Fcs
Offutt AFB
Omaha, NB 68113
ATTN: JPST MAJ. J. S. Green

CHIEF
Livermore Division FLD Command DNA
Lawrence Livermore Laboratory
P. O. Box 808
Livermore, CA 94550
ATTN: FCPRL

COMMANDER
National Military Comd Sys Support Ctr
Pentagon
Washington, D. C. 20301
ATTN: B211

COMMANDER
National Military Comd Sys Support Ctr
Pentagon
Washington, D. C. 20301
ATTN: DP Director for CSPO

DIRECTOR
National Security Agency
National Security Agency
Ft. George G. Meade, Md. 20755
ATTN: W14 Pat Clark

DIRECTOR
National Security Agency
Ft. George G. Meade, Md. 20755
ATTN: Frank Leonard

OJCS/J-3
The Pentagon
Washington, D. C. 20301
ATTN: J-3 OPS ANAL BR. COL. Longsberry

OJCS/J-6
The Pentagon
Washington, D. C. 20301
ATTN: J-6

DIRECTOR
Telecommunications & Comd & Con Sys
Washington, D. C. 20301
ATTN: ASST DIR Info & Space Sys

DISTRIBUTION LIST
(Continued)

DIRECTOR
Telecommunications & Comd & Con Sys
Washington, D. C. 20301
ATTN: DEP ASST. SEC Sys

Weapons Systems Evaluation Group
400 Army Navy Drive
Arlington, VA 22202
ATTN: DOCUMENT CONTROL

DIRECTOR
BMD Advanced Tech Ctr.
Huntsville Office
P. O. Box 1500
Huntsville, AL 35807
ATTN: ATC-T Melvin T. Capps

MANAGER
BMD Program Office
1300 Wilson Blvd.
Arlington, VA 22209
ATTN: Plans Division

MANAGER
BMD Program Office
1300 Wilson Blvd.
Arlington, VA 22209
ATTN: DACS-BMS Julian Davidson

COMMANDER
Harry Diamond Laboratories
2800 Powder Mill Road
Adelphi, MD. 20783
ATTN: AMXDO-NP

COMMANDER
TRASANA
White Sands Missle Range, NM 88002
ATTN: EAB

DIRECTOR
U. S. Army Baliistic Research Labs
Aberdeen Proving Ground, MD. 21005
ATTN: AM-CA Franklin E. Niles

U. S. Army Communications CMD
C-E Services Division
Pentagon Rm. 2D513
Washington, D. C. 20310
ATTN: CEAD

DISTRIBUTION LIST
(Continued)

COMMANDER
U. S. Army Electronics Command
Fort Monmouth, J. J. 07703
ATTN: AMSEL-TL-ENV HANS A. BOMKE

COMMANDER
U. S. Army Material Command
5001 Eisenhower Avenue
Alexandria, VA 22333
ATTN: AMCRD-WN-RE JOHN F. CORRIGAN

COMMANDER
U. S. Army Material Command
Foreign and Scientific Tech Center
220 7th St. N. E.
Charlottesville, VA 22901
ATTN: P. A. Crowley

COMMANDER
U. S. Army Material Command
Foreign and Scientific Tech Center
220 7th St. N. E.
Charlottesville, VA 22901
ATTN: R. Jones

COMMANDER
U. S. Army Missile Command
Redstone Arsenal
Huntsville, AL 35809
ATTN: AMSMI-YTT W. G. Preussel, Jr.

COMMANDER
U. S. Army Nuclear Agency
Fort Bliss, TX 79916
ATTN: CDINS-E

COMMANDER
U. S. Army Nuclear Agency
Fort Bliss, TX 79916
ATTN: USANUA-W. J. Berbert

CHIEF OF Naval Research
Department of the Navy
Arlington, VA 22217
ATTN: CODE 464 Jacob L. Warner

Chief of Naval Research
Department of the Navy
Arlington, VA 22217
ATTN: CODE 464 Thomas P. Quinn

DISTRIBUTION LIST
(Continued)

COMMANDER
Naval Air Systems Command
Headquarters
Washington, D. C. 21360
ATTN: AIR 5381

COMMANDER
Naval Electronics Systems Command
Naval Electronic Systems CMD HQS
Washington, D. C. 20360
ATTN: NAVALEX 034 T. Barry Hughes

COMMANDER
Naval Electronics Systems Command
Naval Electronic Systems CMD HQS
Washington, D. C. 20360
ATTN: PME 106-1 Satellite Comm Project Off

COMMANDER
Naval Electronics Systems Command
Naval Electronic Systems CMD HQS
Washington, D. C. 20360
ATTN: John E. Doncarlos

COMMANDER
Naval Electronics Systems Command
Naval Electronic Systems CMD HQS
Washington, D. C. 20360
ATTN: PME 117

COMMANDER
Naval Electronics Laboratory Center
San Diego, CA 92152
ATTN: William F. Moler

COMMANDER
Naval Electronics Laboratory Center
San Diego, CA 92152
ATTN: CODE 2200 1 Verne E. Hildebrand

COMMANDER
Naval Electronics Laboratory Center
San Diego, CA 92152
ATTN: R. Eastman

COMMANDING OFFICER
Naval Intelligence Support CTR
4301 Suitland Road, Bldg. 5
Washington, D. C. 20390
ATTN: Mr. Dubbin Stic 12

DISTRIBUTION LIST
(Continued)

DIRECTOR
Naval Research Laboratory
Washington, D. C. 20375
ATTN: HDQ COMM DIR Bruce Wald

DIRECTOR
Naval Research Laboratory
Washington, D. C. 20375
ATTN: CODE 5460 Radio Propagation BR

DIRECTOR
Naval Research Laboratory
Washington, D. C. 20375
ATTN: CODE 7127, Charles Y. Johnson

DIRECTOR
Naval Research Laboratory
Washington, D. C. 20375
ATTN: CODE 7701 Jack D. Brown

DIRECTOR
Naval Research Laboratory
Washington, D. C. 20375 — 25 copies (if unclassified)
ATTN: CODE 7700, Division Superintendent — 1 copy (if classified)

DIRECTOR
Naval Research Laboratory
Washington, D. C. 20375 — 150 copies (if unclassified)
ATTN: CODE 7750, Branch Head — 1 copy (if classified)

COMMANDER
Naval Space Surveillance System
Dahlgren, VA 22448
ATTN: CAPT. J. H. Burton

COMMANDER
Naval Surface Weapons Center
White Oak, Silver Spring MD. 20910
ATTN: CODE 730 Tech. Lib.

COMMANDER
Naval Surface Weapons Center
White Oak, Silver Sprin, Md. 20910
ATTN: CODE 1224 Navy Nuc Prgms Off

DIRECTOR
Strategic Systems Project Office
Navy Department
Washington, D. C. 20376
ATTN: NSP-2141

DISTRIBUTION LIST
(Continued)

COMMANDER
ADC/AD
ENT AFB CO 80912
ATTN: ADDA

AF Cambridge Rsch Labs, AFSC
L. G. Hanscom Field
Bedford, MA 01730
ATTN: LKB Kenneth S. W. Champion

AF Cambridge Rsch Labs, AFSC
L. G. Hanscom Field
Bedford, MA 01730
ATTN: OPR Hervey P. Gauvin

AF Cambridge Rsch Labs, AFSC
L. G. Hanscom Field
Bedford, MA 01730
ATTN: OPR James C. Ulwick

AF Weapons Laboratory, AFSC
Kirtland AFB, NM 87117
ATTN: DYT LT Mark A. Fry

AF Weapons Laboratory, AFSC
Kirtland AFB, NM 87117
ATTN: DYT CAPT Wittwer

AF Weapons Laboratory, AFSC
Kirtland AFB, NM 87117
ATTN: John M. Kamm SAS

AF Weapons Laboratory, AFSC
Kirtland AFB, NM 87117
ATTN: SUL

AF Weapons Laboratory, AFSC
Kirtland AFB, NM 87117
ATTN: SAS John M. Kamm

AFTAC
Patrick AFB, FL 32925
ATTN: TF MAJ. E. Hines

AFTAC
Patrick AFB, FL 32925
ATTN: TF/CAPT. Wiley

DISTRIBUTION LIST
(Continued)

AFTAC
Patrick AFB, FL 32925
ATTN: TN

Air Force Avionics Laboratory, AFSC
Wright-Patterson AFB, OH 45433
ATTN: AFAL AVWE Wade T. Hunt

Assistant Chief of Staff
Studies and Analysis
Headquarters, U. S. Air Force
Washington, D. C. 20330

Headquarters
Electronic Systems Division, (AFSC)
L. G. Hanscom Field
Bedford, MA 01730
ATTN: XRE LT. Micheals

Headquarters
Electronic Systems Division, (AFSC)
L. G. Hanscom Field
Bedford, MA 01730
ATTN: LTC J. Morin CDEF XRC

Headquarters
Electronic Systems Division, (AFSC)
L. G. Hanscom Field
Bedford, MA 01730
ATTN: YSEV

COMMANDER
Foreign Technology Division, AFSC
Wright-Patterson AFB, OH 45433
ATTN: TD-BTA, LIBRARY

HQ USAF/RD
Washington, D. C. 20330
ATTN: RDQ

COMMANDER
Rome Air Development Center, AFSC
Griffiss AFB, N. Y. 13440
ATTN: EMTLD Doc Library

COMMANDER IN CHIEF
Strategic Air Command
Offutt AFB, NB 68113
ATTN: XPFS MAJ. Brian G. Stephan

DISTRIBUTION LIST
(continued)

5441ES
Offutt AFB, NB 68113
ATTN: RDPO LT. Alan B. Merrill

Los Alamos Scientific Laboratory
P. O. Box 1663
Los Alamos, NM 87544
ATTN: DOC CON for Eric Lindman

Los Alamos Scientific Laboratory
P. O. Box 1663
Los Alamos, NM 87544
ATTN: DOC CON for H. M. Peek

Los Alamos Scientific Laboratory
P. O. Box 1663
Los Alamos, NM 87544
ATTN: DOC CON for R. F. Taschek

Sandia Laboratories
P. O. Box 5800
Albuquerque, NM 87115
ATTN: DOC CON for A. Dean Thornbrough

Sandia Laboratories
P. O. Box 5800
Albuquerque, NM 87115
ATTN: DOC CON for W. D. Brown

Sandia Laboratories
P. O. Box 5800
Albuquerque, NM 87115
ATTN: DOC CON for D. A. Dahlgren, ORG 1722

Sandia Laboratories
P. O. Box 5800
Albuquerque, NM 87115
ATTN: DOC CON for J. P. Martin, ORG 1732

University of California
Lawrence Livermore Laboratory
P. O. Box 808
Livermore, CA 94550
ATTN: Tech Info Dept L-3

Department of Commerce
National Oceanic & Atmospheric Admin.
Environmental Research Laboratories
Boulder, CO 80302
ATTN: Joseph H. Pope

DISTRIBUTION LIST
(continued)

Department of Commerce
National Oceanic & Atmospheric Admin
Environmental Research Laboratories
Boulder, CO 80302
ATTN: C. L. Rufenach

Department of commerce
Office of Telecommunications
Instatute for Telecom Science
Boulder, CO 80302
ATTN: Glenn Falcon

Department of Commerce
Office of Telecommunications
Instatute for Telecom science
Boulder, CO 80302
ATTN: William F. Utlaut

Department of Commerce
Office of Telecommunications
Institute for Telecom Science
Boulder, CO 80302
ATTN: G. Reed

Department of Commerce
Office of Telecommunications
Institute for Telecom Science
Boulder, CO 80302
ATTN: L. A. Berry

Department of Transportation
Transportation Rsch. System Center
Kendall Square
Cambridge, MA 02142
ATTN: TER G. Harowles

NASA
Goddard Space Flight Center
Greenbelt, MD 20771
ATTN: CODE 750 T. Golden

NASA
600 Independence Ave., S. W.
Washington, D. C. 20546
ATTN: M. Dubin

Aerospace Corporation
P. O. Box 92957
Los Angeles, CA 90009
ATTN: T. M. Salmi

DISTRIBUTION LIST
(Continued)

Aerospace Corporation
P. O. Box 92957
Los Angeles, CA 90009
ATTN: S. P. Bower

Aerospace Corporation
P. O. Box 92957
Los Angeles, CA 90009
ATTN: V. Josephson

Aerospace Corporation
P. O. Box 92957
Los Angeles, CA 90009
ATTN: SMFA for PWW

Analytical Systems Corporation
25 Ray Avenue
Burlington, MA 01803
ATTN: Radio Sciences

Avco-Everett Research Laboratory, Inc.
2385 Reverse Beach Parkway
Everett, MA 02149
ATTN: Richard M. Patrick

Bell Telephone Laboratories, Inc.
Mountain Avenue
Murray Hill, N.J. 07974
ATTN: Norman J. Zabusky

Boeing Company, The
P. O. Box 3707
Seattle, WA 98124
ATTN: D. Murray

Boeing Company, The
P. O. Box 3707
Seattle, WA 98124
ATTN: Glen Keister

Brown Engineering Compnay, Inc.
Cummings Research Park
Huntsville, AL 35807
ATTN: David Lambert MS 18

California at San Diego, Univ of
Building 500 Mathews Campus
3172 Miramar Road
La Jolla, CA 92037
ATTN: Henry G. Booker

DISTRIBUTION LIST
(Continued)

Calspan Corporation
P. O. Box 235
Buffalo, N. Y. 14221
ATTN: Romeo A. Deliberis

Computer Sciences Corporation
P. O. Box 530
6565 Arlington, VA 22046
ATTN: H. Blank

Computer Sciences Corporation
P. O. Box 530
6565 Arlington Blvd.
Falls Church, VA. 22046
ATTN: Barbara F. Adams

Comsat Laboratories
P. O. Box 115
Clarksburg, MD. 20734
ATTN: R. R. Taur

Cornel University
Department of Electrical Engineering
Ithaca, N. Y. 14850
ATTN: D. T. Farley, Jr.

ESL, INC.
495 Java Drive
Sunnyvale, CA 93102
ATTN: J. Roberts

ESL, Inc.
495 Java Drive
Sunnyvale, CA 93102
ATTN: V. L. Mower

ESL, Inc.
495 Java Drive
Sunnyvale, CA 93102
ATTN: James Marshall

ESL, Inc.
495 Java Drive
Sunnyvale, CA 93102
ATTN: R. K. Stevens

DISTRIBUTION LIST
(Continued)

General Electric Company
Temp-Center for Advanced Studies
816 State Street
Santa Barbara, CA 93102
ATTN: Don Chandler

General Electric Company
Tempo-Center for Advanced Studies
816 State Street (P.O. Drawer QQ)
Santa Barbara, CA 93102
ATTN: DASIAC

General Electric Company
P. O. Box 1122
Syracuse, N. Y. 13201
ATTN: F. A. Reibert

General Electric Company
Tempo-Center for Advanced Studies
816 State Street (P. O. Drawer QQ)
Santa Barbara, CA 93102
ATTN: Tim Stephens

General Research Corporation
P. O. Box 3587
Santa Barbara, CA 93105
ATTN: John Ise, Jr.

Geophysical Institute
University of Alaska
Fairbanks, AK 99701
ATTN: Technical Library

Geophysical Institute
University of Alaska
Fairbanks, AK 99701
ATTN: Neil Brown

Geophysical Institute
University of Alaska
Fairbanks, AK 99701
ATTN: T. N. Davis

GTE Sylvania, Inc.
189 B Street
Needham Heights, MA 02194
ATTN: Marshal Cross

DISTRIBUTION LIST
(Continued)

HRB-Singer, Inc.
Science Park, Science Park Road
P. O. Box 60
State College, PA 16801
ATTN: Larry Feathers

Illinois, University of
Department of Electrical Engineering
Urbana, IL 61801
ATTN: K. C. Yeh

Institute for Defense Analyses
400 Army-Navy Drive
Arlington, VA 22202
ATTN: Ernest Bauer

Institute for Defense Analyses
400 Army-Navy Drive
Arlington, VA 22202
ATTN: Hans Wolfhard

Institute for Defense Analyses
400 Army-Navy Drive
Arlington, VA 22202
ATTN: J. M. Aein

Institute for Defense Analyses
400 Army-Navy Drive
Arlington, VA 22202
ATTN: Joel Bengston

Intl Tel & Telegraph Corporation
500 Washington Avenue
Nutley, N. J. 07110
ATTN: Technical Library

Itt Electro-Physics Laboratories, Inc.
9140 Old Annapolis Road
Columbia, MD. 21043
ATTN: John M. Kelso

John Hopkins University
Applied Physics Laboratory
8621 Georgia Avenue
Silver Spring, MD 20910
ATTN: Document Librarian

DISTRIBUTION LIST
(Continued)

Lockheed Missiles & Space Co., Inc.
P. O. Box 504
Sunnyvale, CA 94088
ATTN: Dept 60-12

Lockheed Missiles and Spate Company
3251 Hanover Street
Palo Alto, CA 94304
ATTN: Billy M. McCormac, Dept 52-14

Lockheed Missiles and Space Company
3251 Hanover Street
Palo Alto, CA 94304
ATTN: Martin Walt, Dept 52-10

Lockheed Missiles and Space Company
3251 Hanover Street
Palo Alto, CA 94304
ATTN: Richard G. Johnson, Dept 52-12

M.I.T. Lincoln Laboratory
P. O. Box 73
Lexington, MA 02173
ATTN: Mr. Walden, X113

M.I.T. Lincoln Laboratory
P. O. Box 73
Lexington, MA 02173
ATTN: D. Clark

M.I.T. Lincoln Laboratory
P. O. Box 73
Lexington, MA 02173
ATTN: James H. Pannell L-246

M.I.T. Lincoln Laboratory
P. O. Box 73
Lexington, MA 02173
ATTN: Lib A-082 for David M. Towle

Martin Marietta Corporation
Denver Distribution
P. O. Box 179
Denver, CO 80201
ATTN: Special Projects Program 248

Maxwell Laboratories, Inc.
9244 Balboa Avenue
San Diego, CA 92123
ATTN: A. J. Shannon

DISTRIBUTION LIST
(Continued)

Maxwell Laboratories, Inc.
9244 Balboa Avenue
San Diego, CA 92123
ATTN: V. Fargo

Maxwell Laboratories, Inc.
9244 Balboa Avenue
San Diego, CA 92123
ATTN: A. N. Rostocker

McDonnell Douglas Corporation
5301 Bolsa Avenue
Huntington Beach, CA 92647
ATTN: J. Moule

McDonnell Douglass Corporation
5301 Bolsa Avenue
Huntingson Beach CA 92647
ATTN: N. Harris

McDonnell Douglas Corporation
5301 Bolsa Avenue
Huntington Beach, CA 92647
ATTN: Tech Library Services

Mission Research Corporation
735 State Street
Santa Barbara, CA 93101
ATTN: Ralph Kilb

Mission Research Corporation
735 State Street
Santa Barbara, CA 93101
ATTN: R. Hendrick

Mission Research Corporation
735 State Street
Santa Barbara, CA 93101
ATTN: Conrad L. Longmire

Mission Research Corporation
735 State Street
Santa Barbara, CA 93101
ATTN: R. E. Rosenthal

Mission Research Corporation
735 State Street
Santa Barbara, CA 93101
ATTN: R. Bogusch

DISTRIBUTION LIST
(Continued)

Mission Research Corporation
735 State Street
Santa Barbara, CA 93101
ATTN: David Sowle

Mission Research Corporation
735 State Street
Santa Barbara, CA 93101
ATTN: M. Scheibe

Mission Research Corporation
735 State Street
Santa Barbara, CA 93101
ATTN: P. Fischer

Mitre Corporation, The
Route 62 and Middlesex Turnpike
P. O. Box 208
Bedford, MA 01730
ATTN: S. A. Morin M/S

Mitre Corporation, The
Route 62 and Middlesex Turnpike
P. O. Box 208
Bedford, MA 01730
ATTN: Chief Scientist W. Sen

Mitre Corporation, The
Route 62 and Middlesex Turnpike
P. O. Box 208
Bedford, MA 017330
ATTN: G. Harding

Mitre Corporation, The
Westgate Research Park
1820 Dolley Madison Blvd.
McLean, VA 22101
ATTN: Allen Schneider

North Carolina State Univ at Raleigh
North Carolina State Univ Campus
Raleigh, N. C. 27507
ATTN: SEC Officer for Walter A. Flood

Pacific-Sierra Research Corp.
1456 Cloverfield Blvd.
Santa Monica, CA 90404
ATTN: E. C. Field, Jr.

DISTRIBUTION LIST
(Continued)

Philco-Ford Corporation
Western Development Laboratories Div
3939 Fabian Way
Palo Alto, CA 94303
ATTN: J. T. Mattingley MS X22

Photometrics, Inc.
442 Marrett Road
Lexington, MA 02173
ATTN: Irving L. Kofsky

Physical Dynamics, Inc.
P. O. Box 1069
Berkeley, CA 94701
ATTN: Joseph B. Workman

R & D Associates
P. O. Box 3580
Santa Monica, CA 90403
ATTN: Robert E. Lelevier

R & D Associates
P. O. Box 3580
Santa Monica, CA 90403
ATTN: Forest Gilmore

R & D Associates
P. O. Box 3580
Santa Monica, CA 90403
ATTN: Richard Latter

R & D Associates
P. O. Box 3580
Santa Monica, CA 90403
ATTN: William B. Wright, Jr.

Rand Corporation, The
1700 Main Street
Santa Monica, CA 90406
ATTN: Cullen Crain

Science Applications, Inc.
P. O. Box 2351
La Jolla, CA 92038
ATTN: Daniel A. Hamlin

Science Applications, Inc.
P. O. Box 2351
La Jolla, CA 92038
ATTN: D. Sachs

DISTRIBUTION LIST
(Continued)

Science Applications, Inc.
P. O. Box 2351
La Jolla, CA 92038
ATTN: E. A. Staraker

Stanford Research Institute
333 Ravenswood Avenue
Menlo Park, CA 94025
ATTN: L. L. Cobb

Stanford Research Institute
333 Ravenswood Avenue
Menlo Park, CA 94025
ATTN: Walter G. Chestnut

Stanford Research Institute
333 Ravenswood Avenue
Menlo Park, CA 94025
ATTN: Donald Neilson

Stanford Research Institute
333 Ravensweed Avenue
Menlo Park, CA 94025
ATTN: David A. Johnson

Stanford Research Institute
333 Ravenswood Avenue
Menlo Park, CA 94025
ATTN: Charles L. Rino

Stanford Research Institute
333 Ravenswood Avenue
Menlo Park, CA 94025
ATTN: E. J. Fremouw

Stanford Research Institute
306 Wynn Drive, N. W.
Huntsville, AL 35805
ATTN: Dale H. Divis

Tri-Com, Inc.
12216 Parklawn Place
Rockville, MD 20852
ATTN: Darrel Murray

DISTRIBUTION LIST
(Continued)

TRW Systems Group
One Space Park
Redondo Beach, CA 90278
ATTN: P. H. Katsos

TRW Systems Group
One Space Park
Redondo Beach, CA 90278
ATTN: J. W. Lowry